



The global aerosol–climate model ECHAM6.3–HAM2.3

– Part 1: Aerosol evaluation

Ina Tegen¹, David Neubauer², Sylvaine Ferrachat², Colombe Siegenthaler-Le Drian³, Isabelle Bey^{3,a}, Nick Schutgens^{4,b}, Philip Stier⁴, Duncan Watson-Parris⁴, Tanja Stanelle², Hauke Schmidt⁵, Sebastian Rast⁵, Harri Kokkola⁶, Martin Schultz⁷, Sabine Schroeder⁷, Nikos Daskalakis⁸, Stefan Barthel¹, Bernd Heinold¹, and Ulrike Lohmann²

¹Leibniz Institute for Tropospheric Research, Leipzig, Germany

²Institute of Atmospheric and Climate Science, ETH Zurich, Zurich, Switzerland

³Centre for Climate Systems Modeling (C2SM), ETH Zurich, Zurich, Switzerland

⁴Department of Physics, University of Oxford, Oxford, UK

⁵Max Planck Institute for Meteorology, Hamburg, Germany

⁶Atmospheric Research Centre of Eastern Finland, Finnish Meteorological Institute, Kuopio, Finland

⁷Forschungszentrum Juelich, Juelich, Germany

⁸Laboratory for Modeling and Observation of the Earth System (LAMOS), Institute of Environmental Physics (IUP),

University of Bremen, Bremen, Germany

^anow at: MeteoSwiss, Geneva, Switzerland

^bnow at: Faculty of Life and Earth Sciences, Vrije Universiteit, Amsterdam, the Netherlands

Correspondence: I. Tegen (itegen@tropos.de)

Received: 20 September 2018 – Discussion started: 11 October 2018

Revised: 23 January 2019 – Accepted: 7 February 2019 – Published: 24 April 2019

Abstract. We introduce and evaluate aerosol simulations with the global aerosol–climate model ECHAM6.3–HAM2.3, which is the aerosol component of the fully coupled aerosol–chemistry–climate model ECHAM–HAMMOZ. Both the host atmospheric climate model ECHAM6.3 and the aerosol model HAM2.3 were updated from previous versions. The updated version of the HAM aerosol model contains improved parameterizations of aerosol processes such as cloud activation, as well as updated emission fields for anthropogenic aerosol species and modifications in the online computation of sea salt and mineral dust aerosol emissions. Aerosol results from nudged and free-running simulations for the 10-year period 2003 to 2012 are compared to various measurements of aerosol properties. While there are regional deviations between the model and observations, the model performs well overall in terms of aerosol optical thickness, but may underestimate coarse-mode aerosol concentrations to some extent so that the modeled particles are smaller than indicated by the observations. Sulfate aerosol measurements in the US and

Europe are reproduced well by the model, while carbonaceous aerosol species are biased low. Both mineral dust and sea salt aerosol concentrations are improved compared to previous versions of ECHAM–HAM. The evaluation of the simulated aerosol distributions serves as a basis for the suitability of the model for simulating aerosol–climate interactions in a changing climate.

1 Introduction

The increase in the positive radiative forcing of anthropogenic greenhouse gases and tropospheric ozone is partly offset by aerosols imposing a negative radiative forcing (Boucher et al., 2013; Myhre et al., 2013). Global aerosol–chemistry–climate models are key tools in the attribution and projection of the role of aerosols in the climate system. In general, aerosol components such as black and organic carbon, sulfate, mineral dust, and sea salt are considered in such models, as are their sources, sinks, transport, and chem-

ical and microphysical transformations. Considerable efforts have been made over the last decades to improve the incorporation of the relevant aerosol processes in climate models that control the distribution and effects of these species in the atmosphere. However, uncertainties in quantifications of aerosol–radiation interactions and aerosol–cloud interactions remain large. Further development and evaluation of global climate–aerosol–chemistry models is thus necessary to reduce such uncertainties and provide a basis for investigating the response of the coupled aerosol–climate system in a changing climate.

In addition to the host climate models, embedded aerosol–chemistry models are continuously refined and further developed as new processes are included and process representations are improved. The increasing complexity of these models requires systematic documentation of the different existing versions. The ECHAM–HAM model, consisting of the atmospheric general circulation model ECHAM and the aerosol module HAM, has previously been widely used in process studies (Lohmann and Hoose, 2009; Folini and Wild, 2011; Kazil et al., 2012; Peters et al., 2014; Neubauer et al., 2014; Schutgens et al., 2014; Gasparini and Lohmann, 2016; Lohmann and Neubauer, 2018) and contributed extensively to model evaluation and intercomparison studies (Textor et al., 2006; Textor et al., 2007; Kulmala et al., 2011; Huneeus et al., 2011; Stier et al., 2013; Jiao et al., 2014). The latest version of the ECHAM–HAMMOZ model (version ECHAM6.3–HAM2.3–MOZ1.0) combines the most recent versions ECHAM (ECHAM6; Stevens et al., 2013), the aerosol module HAM2 (Zhang et al., 2012), and the atmospheric trace gas chemistry module MOZ (described in Rast et al., 2014). The aerosol (HAM) and the chemistry (MOZ) modules can either be used interactively or independently of each other. The coupled ECHAM6–HAMMOZ model is described in detail in Schultz et al. (2018). The notation ECHAM–HAMMOZ is used when both the aerosol and chemistry modules are used interactively in combination with the climate model ECHAM, and the notations ECHAM–HAM and ECHAM–MOZ apply when only the aerosol and chemistry modules, respectively, are used individually. The HAM and MOZ modules share a common interface with ECHAM6 and consistent representation of common processes (e.g., emissions and deposition of trace gases and aerosols, as well as cloud microphysics) and the associated routines. The details of the chemistry module MOZ and evaluation of the ECHAM6.3–HAM2.3–MOZ1.0 model configuration are described in Schultz et al. (2018). In this study only the aerosol module HAM is used such that the aerosol computations are fully interactive, while the oxidant fields that would be computed interactively in the HAMMOZ setup are prescribed. Cloud processes and cloud–aerosol interactions, as well as direct radiative forcing simulated in ECHAM6.3–HAM2.3, are evaluated in a companion study by Neubauer et al. (2019).

Here the emphasis is placed on the description and evaluation of the aerosol distributions simulated by ECHAM6.3–HAM2.3 to provide a basic quantitative evaluation against a suite of observations of the different aspects of aerosol distributions. We focus on the model version using the modal aerosol computing microphysical processes such as nucleation, coagulation, and condensational growth by the modal scheme M7 (Vignati et al., 2004; Zhang et al., 2012; Neubauer et al., 2014; Schutgens et al., 2014). Alternatively the aerosol microphysical processes can be described by the sectional or bin aerosol scheme SALSA in the ECHAM6.3–HAM2.3–SALSA configuration, which is described in Kokkola et al. (2008, 2018).

2 Model description

2.1 Model development overview

The aerosol module HAM was first implemented in the fifth generation of the atmospheric general circulation model ECHAM (ECHAM5; Roeckner et al., 2003) by Stier et al. (2005). In the past years, ECHAM–HAM has undergone substantial software restructuring and scientific development. The host atmospheric model ECHAM was considerably further developed and improved, leading to the version ECHAM6 (Stevens et al., 2013). The HAM module has been continuously expanded with new processes based on the version HAM2 as described in Zhang et al. (2012). The MOZ module for tropospheric and stratospheric chemistry was subsequently introduced in a joint effort by several institutions. The first version of the fully coupled aerosol–chemistry–climate model ECHAM5–HAMMOZ was documented in Pozzoli et al. (2008). The latest version of the ECHAM–HAMMOZ model has been developed as an international collaboration. The model is currently hosted by ETH Zurich (Switzerland) and TROPOS in Leipzig (Germany) (<https://redmine.hammoz.ethz.ch/projects/hammoz>, last access: 1 March 2019).

The recent generation of the ECHAM–HAMMOZ model is constructed in a more modular approach compared to previous versions to minimize interactions of the aerosol module with the host general circulation model. ECHAM6 now provides a generic sub-model interface, i.e., a specific Fortran module, which contains all calls to the aerosol and chemistry routines. This facilitates simultaneous development and separation of the climate (ECHAM), chemistry (MOZ), and aerosol (HAM) modules. The structure of the aerosol and gas-phase chemistry codes was harmonized so that both components use the same routines for emissions, dry deposition, and washout (with adaptations as necessary due to the differences in the respective processes). The tracer interface for the definition of chemical species, including their physical and chemical properties, and the concept of output streams to allow for flexible output of tracer diagnostics including tracer

mass mixing ratios, emission, dry deposition, and washout mass fluxes for selected tracers was further extended. This allows us, for example, to distinguish between species that define physical and chemical aerosol properties and tracers that essentially provide the memory for advected compounds. While for gas-phase compounds species and tracers are identical, individual aerosol species can be contained in several tracers such as different aerosol modes or size bins.

2.2 ECHAM6

ECHAM is an atmospheric general circulation model developed by the Max Planck Institute for Meteorology in Hamburg, Germany. The model utilizes a spectral transform dynamical core and a semi-Lagrangian tracer transport scheme in flux form (Lin and Rood, 1996). Vertical transport considers turbulent mixing, moist convection (shallow, deep, and mid-level convection), and momentum transport by gravity waves. Convection is parameterized via the mass-flux schemes by Tiedtke (1989) and Nordeng (1994). Parameterization of sub-grid-scale stratiform clouds uses the scheme of Sundqvist et al. (1989). Cloud liquid water content and cloud ice mixing ratios are computed prognostically (Lohmann and Roeckner, 1996). In the standard setup that is used in this work the spectral resolution is T63, corresponding to $1.875^\circ \times 1.875^\circ$ horizontal resolution. The vertical resolution is 47 layers with a top layer at 0.1 hPa.

The current version ECHAM6 is described in detail in Stevens et al. (2013). The vertical discretization within the troposphere (in particular in the upper troposphere and lower stratosphere) is slightly different in ECHAM6 compared to the previous version ECHAM5. The representation of convective triggering has been improved, and the tuning of various model parameters was adjusted. ECHAM6 is frequently used in a middle-atmosphere configuration with the two vertical grids L47 and L95 that resolve the atmosphere from the surface up to 0.01 hPa (roughly 80 km). Radiative transfer in ECHAM6 is computed using the PSrad/RRTMG (a rapid radiative transfer model for GCMs) (Iacono et al., 2008; Pinchus and Stevens, 2013) radiation package, which considers 16 bands for the shortwave (820 to $50\,000\text{ cm}^{-1}$) and 14 bands for the longwave (10 to 3000 cm^{-1}) parts of the spectrum, respectively. Optical properties of clouds are precalculated for each band of the RRTMG scheme using Mie theory and read from lookup tables. The cloud droplet number concentrations are prescribed differently over land and ocean in the case that ECHAM is used without the HAM aerosol module. In this case climatological average aerosol optical properties by Kinne et al. (2013) are used in radiative transfer computations in ECHAM6. Trace gas concentrations of long-lived greenhouse gases are specified in the model if used without a chemistry module. ECHAM6 includes the land surface model JSBACH (Reick et al., 2013), which assumes that each land grid cell is composed of two fractions representing bare and vegetated soil surfaces. The vegetated

surface fraction is further subdivided into tiles for each of the plant functional types distinguished in JSBACH. Soil hydrology is represented with a single-layer bucket model.

The variability in the tropics continues to be well represented in ECHAM6 similarly to its predecessor ECHAM5 (Roeckner et al., 2003). This includes, e.g., intraseasonal variability, the quasi-biennial oscillation, and some aspects of the El Niño Southern Oscillation (ENSO). The representation of extratropical circulation is clearly improved in ECHAM6 (Stevens et al., 2013).

Compared to the original version of ECHAM6 the updates in the current version ECHAM6.3 include some modifications in the radiation and land surface schemes and an improved sub-model interface. The influence of orography on surface roughness was replaced by an aerodynamic roughness determined by vegetation cover.

ECHAM drives the aerosol and chemistry modules through the generic sub-model interface by providing meteorological conditions such as wind, temperature, pressure, humidity, and conditions related to the land surface (taken from JSBACH) such as leaf area index (LAI). Aerosols and their precursors are transported analogous to the tracer transport of water vapor and cloud water in ECHAM.

2.3 HAM2

The Hamburg Aerosol Model (HAM) (Stier et al., 2005) computes the evolution of an aerosol mixture considering the species sulfate, black carbon (BC), organic carbon (OC), sea salt, and mineral dust. Coupled to an atmospheric general circulation model such as ECHAM, the development of the mass and number concentrations of aerosols is computed taking into account physical and chemical particle processes. In turn, the effects of aerosols on clouds and radiation are computed prognostically in the coupled ECHAM–HAM. The second model version HAM2, containing new updates in parameterizations of particle nucleation and growth, emission calculations for natural aerosol species, and aerosol–cloud interactions, is described and evaluated by Zhang et al. (2012). The relative importance of the individual aerosol processes in ECHAM5–HAM2 has been evaluated by Schutgens et al. (2014).

The default version of HAM describes the aerosol size spectrum by the modal M7 aerosol model (Vignati et al., 2004). Aerosols are simulated as the superposition of seven lognormal modes: nucleation mode, soluble (mixed) and insoluble Aitken, accumulation, and coarse modes (Table 1). The aerosol distribution in each mode is described by the aerosol number, the median radius, and the standard deviation. The standard deviation is 1.59 for the nucleation, Aitken, and accumulation modes and 2.00 for the coarse modes. The median radius of each mode is calculated from the aerosol number and aerosol mass, which are transported as tracers within the respective mode. Each aerosol mode is assumed to be internally mixed such that individual particles

in a mode can consist of different species. To be considered soluble, at least one species within a particle must be soluble. Insoluble particles can become mixed (soluble) through the condensation of soluble substances and collisions with mixed particles.

The current version HAM2.3 described here is updated in terms of default settings and model organization, aerosol emissions, water uptake, wet deposition, and aspects of aerosol–cloud interactions compared to the version HAM2.0 described by Zhang et al. (2012). In addition to minor corrections and bug fixes, major changes in HAM2.3 are the following.

- Updates and changes in emissions of aerosols and aerosol precursors from anthropogenic and natural sources (described in detail in section 2.3.1):
 - new emission datasets for anthropogenic emissions of BC, OC, and SO_2 ;
 - updated emission parameterization for mineral dust; and
 - new emission parameterization for sea salt aerosols based on Long et al. (2011) and Sofiev et al. (2011), including parameterization for ocean temperature dependence.
- Modified aerosol–cloud interactions (described in Lohmann and Neubauer, 2018):
 - cloud droplet activation according to Abdul-Razzak and Ghan (2000) based on Köhler theory;
 - updated treatment of cloud droplet number concentrations (CDNCs) detrained from convective clouds;
 - size-dependent in-cloud scavenging by Croft et al. (2010);
 - assuming hexagonal plates as the shape of ice crystals following Pruppacher and Klett (1997);
 - limiting the immersion freezing of black carbon to particles in the accumulation or coarse mode;
 - changed temperature dependence of sticking efficiency for the accretion of ice crystals by snow according to Seifert and Beheng (2006); and
 - optional choice of minimum CDNC as either 40 cm^{-3} or 10 cm^{-3} .

2.3.1 Emissions of aerosol particles and aerosol precursors

The HAM2.3 emission module of primary aerosol particles and gas-phase compounds has been designed such that emissions are specified for individual sectors such as industrial or domestic fossil fuel use in a user-friendly way. An emission input file specifies for each species which emission sectors are considered and how the emission fluxes from these

sources are introduced in the model simulation. For example, all species can be emitted into the lowest model level, a model level corresponding to a specific altitude (as is the case for biomass burning or volcanic emissions), or emitted species can be evenly mixed within the planetary boundary layer. This applies to all emissions from a specific sector. It is also easily possible to apply a scale factor to emission fluxes from a specific sector. This factor can also be used to temporarily turn off individual emission types or sectors.

The default version of ECHAM6.3–HAM2.3 uses the Atmospheric Chemistry and Climate Model Intercomparison Project (ACCMIP) emission dataset (Lamarque et al., 2010) for anthropogenic and biomass burning emissions. It is based on horizontally gridded temporally interpolated monthly mean anthropogenic emissions for the years 1850 to 2000 combined from regional and global inventories, and it is available at 0.5° horizontal grid resolution. SO_2 , BC, and OC emissions are considered for the relevant anthropogenic sectors including agricultural waste burning, aircraft, domestic, energy, industry, ships, transport, and waste. The dataset also contains biomass burning emission fields with historical emissions. These were available at decadal increments and were further interpolated at yearly resolution (see <http://aerocom.met.no/emissions.html>, last access: 1 March 2019, for details) and degraded to the T63 resolution. From 2000 to 2100 this dataset is created from a linear time interpolation of future emission projections. They can be chosen from four different Representative Concentrations Pathways (RCPs), RCP2.6, RCP4.5, RCP6, and RCP8.5 (van Vuuren et al., 2011), denoting the radiative forcing target levels for the year 2100 of 2.6, 4.5, 6, and 8.5 W m^{-2} , respectively. The interpolated anthropogenic ACCMIP and RCP8.5 emissions for the years 1850 and 1960 to 2010 are identical to the AeroCom-II ACCMIP hindcast emission sources available at <http://aerocom.met.no/DATA/download/emissions/AEROCOM-II-ACCMIP/> (last access: 1 March 2019). The biomass burning emissions for forest and grass fires in this emission dataset represent average conditions of the respective decade. Interannual variability in biomass burning is not considered, but the decadal emissions are interpolated for the individual years keeping the same seasonal variability for each year. Injection heights of biomass burning emissions follow the recommendations of Val Martin et al. (2010); 75 % of the emissions are evenly distributed within the planetary boundary layer (PBL), 17 % in the first level, and 8 % in the second level above the PBL

In addition to ACCMIP, other datasets can be used to prescribe species emissions. For biomass burning, the Global Fire Assimilation System (GFAS) (Kaiser et al., 2012) can be used alternatively. GFAS provides gridded biomass burning emissions at 0.5° horizontal grid resolution assimilated from fire radiative power from MODIS satellite observations. Here GFAS version 1.0 is used. For ECHAM6–HAM2.3 the fire emissions for BC, OC, SO_2 , and dimethyl sulfide (DMS) are used from this emission dataset. Combustion rates are

Table 1. Aerosol size modes and species in the M7 aerosol microphysics in HAM. Mode boundaries for the number median particle radii \bar{R} are given for each mode.

Size mode	Soluble	Insoluble
Nucleation ($\bar{R} < 0.005 \mu\text{m}$)	Sulfate	
Aitken ($0.005 \mu\text{m} < \bar{R} < 0.05 \mu\text{m}$)	Sulfate, OC, BC	OC, BC
Accumulation ($0.05 \mu\text{m} < \bar{R} < 0.5 \mu\text{m}$)	Sulfate, OC, BC, sea salt dust	Dust
Coarse ($\bar{R} > 0.5 \mu\text{m}$)	Sulfate, OC, BC, sea salt, dust	Dust

computed using conversion factors for specific land cover. Kaiser et al. (2012) recommend scaling the particulate emissions from the GFAS emission files by the factor 3.4 in order to optimally match observed aerosol optical thickness. This scaling has been shown to perform well for ECHAM–HAM by Veira et al. (2015) for GFAS version 1.1. For the evaluation of ECHAM6.3–HAM2.3 simulations presented in this paper we performed simulations with this scaling factor.

In the HAMMOZ configuration, the secondary volatile organic carbon emissions serving as precursors for secondary organic aerosol (SOA) formation are calculated with an implementation of the MEGAN2.1 model (Guenther et al., 2012; Henrot et al., 2017). SOA formation can be computed with the implementation by O'Donnell et al. (2011), which considers the chemical conversion of volatile organic gases into condensable gases and the partitioning of semi-volatile condensable species into their gas and aerosol phases. The explicit secondary organic aerosol formation routine is not used in the standard setup of ECHAM6.3–HAM2.3. Instead biogenic emissions are treated as primary OC emissions following AeroCom (Dentener et al., 2006).

Mineral dust emissions are computed online using the dust source scheme of Tegen et al. (2002) with modifications as described in Cheng et al. (2008) and Heinold et al. (2016). Dust particle emissions are driven by the 10 m wind speed computed by the atmospheric model. Emission fluxes follow a nonlinear physical process, which depends on surface features and meteorological conditions in potential source areas. HAM prescribes a constant low roughness length of 0.001 cm for the dust emission calculations in potential source areas. The explicit formulation of the saltation process follows Marticorena and Bergametti (1995). A ratio between vertical and horizontal emission fluxes is prescribed for each soil type (Tegen et al., 2002). Dust emissions can only take place in potential dust source areas (usually non-vegetated or low vegetated areas), the distributions of which are taken from an external file derived by Tegen et al. (2002), who identified potential dust source areas using the satellite-derived fraction of vegetated areas and a model-derived distribution of potential vegetation types, as well as the distribution of dried paleolakes. ECHAM6.3–HAM2.3 also includes the option of deriving potential dust sources using the vegetation cover provided by the land component JSBACH, which allows for a full coupling with the land surface scheme

(Stanelle et al., 2014). For Saharan dust sources a satellite-based source mask is implemented (Heinold et al., 2016). It is based on the infrared dust index from the SEVIRI instrument on the geostationary Meteosat Second Generation satellite that allows for the identification of realistic spatiotemporal distributions of dust emission events (Schepanski et al., 2009).

In previous versions, a global correction factor of 0.86 was applied on the threshold friction velocity to account for the inhomogeneity of the factors influencing dust emissions (e.g., surface wind) across the rather coarse model grid boxes. In ECHAM6.3 the surface orography is not taken into account for the aerodynamic surface roughness, in contrast to earlier versions. The subsequent changes in surface wind distributions over dust source areas require additional regional correction factors. For each relevant region that contains dust sources the correction factors are chosen such that the emissions agree with the values by Huneeus et al. (2011). These regional correction factors can be modified via the model namelist. For this model version they are set to 1.45 for North America, South America, and Asia and 1.05 for all other regions for the simulations that were not nudged. For the nudged simulations the correction factors were 1.25 for North America, South America, and Asia and 0.95 for all other regions.

Several parameterizations can be chosen in ECHAM6.3–HAM2.3 for sea salt aerosol emissions. In earlier versions of HAM the parameterization by Guelle et al. (2001) was used in the default setup. In the past years several new sea salt emission parameterizations were developed by different authors mostly based on laboratory measurements. Such measurements also revealed that sea salt aerosol emissions depend to a certain extent on the temperature of the surface water such that at colder temperatures emissions are lower and led to the emission of smaller particles compared to warmer temperatures (e.g., Sofiev et al., 2011). The new standard in ECHAM6.3–HAM2.3 for sea salt emissions uses a parameterization following Long et al. (2011) taking into account temperature dependence according to Sofiev et al. (2011). The performances of the different sea salt emission schemes will be compared in Sect. 5.7. The sea salt emissions now use surface wind speed as well as sea surface temperatures from the model to compute sea salt aerosol emissions for the mixed accumulation and coarse modes. As a marine source

for aerosol precursors, natural emissions of dimethyl sulfide from the marine biosphere are calculated online. Marine DMS emissions depend on DMS concentrations in the seawater and 10 m wind speeds, with the air-sea exchange computed according to Nightingale et al. (2000). DMS concentrations in seawater are taken from Lana et al. (2011).

2.3.2 Aerosol microphysics

Aerosol processes in M7 (Vignati et al., 2004) include the nucleation of sulfuric acid–water droplets, coagulation, the condensation of sulfuric acid, and aerosol water uptake. Nitrate that may also form secondary ammonium nitrate aerosol is currently not considered in HAM. These processes lead to a redistribution of particle numbers and mass among the different modes. For nucleation, the standard version of the model uses the scheme implemented by Kazil et al. (2010), with optional H_2SO_4 organic nucleation based on kinetic nucleation theory (Kuang et al., 2008) or cluster activation. The condensation of sulfuric acid occurs on all preexisting particles of all sizes. Intra-modal and intermodal coagulation is considered for the soluble modes (with the exception of intra-modal coagulation of the mixed coarse mode) and the Aitken insoluble mode (Schutgens et al., 2014). Condensation and coagulation increase the geometric mean radii of the mixed modes, allowing smaller particles to grow into a larger mode. Also, the formation of a monolayer coating of sulfate on an insoluble particle causes it to be moved to a mixed (soluble) mode. The water content of aerosols in each mode is calculated from their chemical composition and the ambient relative humidity using a semi-empirical water uptake scheme based on κ -Köhler theory (Petters and Kreidenweis, 2007) as implemented by O'Donnell et al. (2011).

In the standard released version of ECHAM6.3–HAM2.3, the representation of SOA is based on the assumption that about 15 % of natural terpene emissions at the surface form SOA as described in Dentener et al. (2006). They are assumed to condense immediately on existing aerosol particles and to have identical properties to primary organic aerosols (Stier et al., 2005). As an alternative, an interactive module for the formation of SOA is available (O'Donnell et al., 2011). The SOA precursors considered include biogenic compounds and aromatic compounds from anthropogenic activities and biomass burning. In that scheme, the oxidation of biogenic precursors produces two semi-volatile products that can condense on existing organic-containing particles, while the oxidation of aromatic compounds leads to nonvolatile products that condense immediately. In this work the standard scheme without explicit treatment of SOA formation is used.

2.3.3 Sulfur chemistry

The sulfur chemistry in HAM2 is based on Feichter et al. (1996). Prognostic variables include concentrations of DMS,

SO_2 , and gas- and aqueous-phase sulfate. With the HAM setup (without MOZ), an 8-year mean reanalysis of atmospheric oxidants covering the period 2003–2010 is used. This climatology was constructed by assimilating satellite data into a global model and data assimilation system (Inness et al., 2013). Averaged monthly mean oxidant fields include the hydroxyl radical (OH), hydrogen peroxide (H_2O_2), nitrogen dioxide (NO_2), ozone (O_3), and nitrate radical (NO_3). Sulfuric acid produced from gas-phase chemistry can nucleate to form new particles or condense on existing aerosol particles. Sulfate produced from aqueous-phase chemistry is distributed to preexisting particles in the soluble accumulation and coarse modes. For the HAMMOZ setup the sulfur oxidants are computed online taking into account the full atmospheric chemistry processes described by MOZ (Schultz et al., 2018).

2.3.4 Removal processes

Aerosol particles are removed by sedimentation and dry and wet deposition. The gravitational sedimentation of particles in HAM2 is calculated based on their median size using the Stokes settling velocity (Seinfeld and Pandis, 1998), applying a correction factor according to Slinn and Slinn (1980). Removal of aerosol particles from the lowest model layer by turbulence depends on the characteristics of the underlying surface (Zhang et al., 2012). The aerosol dry deposition flux is computed as the product of tracer concentration, air density, and deposition velocity, depending on the aerodynamic and surface resistances for each surface type considered by ECHAM6.3, and subsequently added up for the fractional surface areas. For wet deposition the in-cloud scavenging scheme from Croft et al. (2010), dependent on the wet particle size, is used. The in-cloud scavenging scheme takes into account scavenging by droplet activation and impaction scavenging in different cloud types, distinguishing between stratiform and convective clouds and warm, cold, and mixed-phase clouds. Below clouds particles are scavenged by rain and snow using a size-dependent below-cloud scavenging scheme (Croft et al., 2009).

2.3.5 Aerosol optical properties

Aerosol optical properties are dynamically computed when using the prognostic aerosol module in ECHAM6.3–HAM2.3. The effective refractive index of each aerosol mode is computed from volume-weighted averages of the refractive indices and Mie-scattering size parameters of the individual components including the water content, assuming internal mixing (Stier et al., 2007; Zhang et al., 2012). For absorbing aerosol species, the complex refractive index for BC at 550 nm is $1.8 + 0.71i$ (Bond and Bergstrom, 2006; Stier et al., 2007) and $1.52 + 0.0011i$ for dust aerosol (Kinne et al., 2013). For dust the parameterization of the complex refractive index is in agreement with the results by Sinyuk et al.

(2003). Extinction cross sections, single-scattering albedos (SSAs), and asymmetry parameters are provided via a lookup table and then remapped onto the bands of the ECHAM radiative transfer model.

2.4 Cloud microphysics

A detailed description of the current implementation of cloud processes and aerosol–cloud interaction is given in Lohmann and Neubauer (2018) and the companion paper Neubauer et al. (2019). The two-moment cloud microphysics scheme in ECHAM, simulating the number concentrations and mass mixing ratios of cloud droplets and ice crystals, is coupled to the aerosol scheme HAM through the processes of cloud droplet activation and ice crystal nucleation (Lohmann et al., 2007), as well as through in-cloud and below-cloud scavenging. Processes such as phase changes, growth by water vapor condensation, deposition and collision processes, and precipitation formation are considered (Zhang et al., 2012). In ECHAM6.3–HAM2.3 contact ice nucleation can be triggered by mineral dust, and dust and black carbon particles can act as ice nuclei. Updates in the cloud scheme in ECHAM6.3–HAM2.3 compared to previous versions include the computation of cloud droplet activation according to Abdul-Razzak and Ghan (2000) based on Köhler theory, limiting the immersion freezing of black carbon to particles in the accumulation or coarse mode, a temperature dependence of sticking efficiency for the accretion of ice crystals by snow following Seifert and Beheng (2006), and an option to choose minimum CDNC as either 40 cm^{-1} or 10 cm^{-1} . Also, inconsistencies were removed, e.g., in the calculation of condensation and cloud cover, as well as in the calculation of the ice crystal number concentration in cirrus clouds. The two-moment cloud microphysics is energy conserving and has been modularized in the updated version.

3 Model setup and experiments

In this publication, we evaluate different aspects of the simulated aerosol distributions for several simulations from the ECHAM6.3–HAM2.3 model. All simulations were performed in T63 spectral resolution, which corresponds to $1.875^\circ \times 1.875^\circ$ horizontal resolution. The vertical resolution is 47 vertical layers with a top at 0.1 hPa. The increased vertical resolution, which affects mostly the stratosphere, has only a limited influence on the global tropospheric aerosol distributions compared to the 31 layers used in the previous version (Zhang et al., 2012; Neubauer et al., 2014). It is used here to ensure consistency with the host model ECHAM. Sea surface temperatures were fixed in the model simulations. The model simulations in this work do not utilize the MOZ sub-model or the SOA scheme.

In the base model setup (NUUDGE), direct comparisons with aerosol observations available at specific dates are fa-

cilitated by simulations in a nudged mode, in which vorticity, divergence, and pressure are relaxed towards the ERA-Interim reanalysis (Berrisford et al., 2011). In the standard setup, the nudging timescales for ECHAM6 are 6 h for vorticity, 48 h for divergence, and 24 h for surface pressure. Sea surface temperatures (SSTs) for this model setup were set to AMIP SSTs for the respective year (Taylor et al., 2000). Since the nudging may have some impact on the computation of the aerosol processes, and as the model will be used in a free mode without nudging in most upcoming studies, the results will be compared for a free, not-nudged simulation (labeled CLIM). The standard model setup includes anthropogenic and biomass burning emissions from the ACCMIP dataset, as described in Sect. 2.3.1, with emission projections based on the RCP4.5 scenario. For the time period 2003–2012 considered in this work, the ACCMIP biomass burning emissions are based on scenarios rather than observations and thus do not vary on daily or interannual timescales, but emissions for each year are interpolated from the decadal emissions. For comparison, aerosol distributions are also simulated with daily available GFAS biomass burning emissions that are based on satellite retrievals (labeled GFAS). As described in Sect. 2.3.1 and suggested by Kaiser et al. (2012), the particulate GFAS emissions for biomass burning are multiplied by a factor of 3.4 in the simulation GFAS. For the evaluation of the new sea salt emission scheme further sensitivity studies are presented, which are described in Sect. 5.7.

The simulations were carried out for the years 2003 to 2012. This time period overlaps with the new reference period as agreed upon in the AeroCom project, which is 2003–2010, and with the previous reference period for the ECHAM5–HAM2 simulations that was 2000–2009. For observations that are time resolved for years within the simulation period, the comparisons are carried out for the actual dates of the observations. Otherwise, the evaluation is for the averaged aerosol properties over the simulation time period.

4 Observations

4.1 Aerosol optical thickness and Ångstrom exponent

Ground-based information on column aerosol properties is available from the global sun photometer network AErosol RObotic NETwork (AERONET; <http://aeronet.gsfc.nasa.gov>, last access: 1 March 2019, Holben et al., 1998). Quality-controlled measurements are routinely taken at several wavelengths, providing information on aerosol optical depth and Ångstrom exponents (AEs), which are an indication for average effective particle sizes in the atmospheric column. These data are widely used as “ground truth” for aerosol properties, e.g., for the evaluation of aerosol model results and satellite retrievals. Model results are compared to Level 2 cloud-screened, 6 h averages of AOT measurements at 675 nm wavelength by linearly interpolating model val-

Table 2. Setup of the simulations with ECHAM6.3–HAM2.3.

Simulation	Description
CLIM	T63; 47 vertical layers; ACCMIP interpolated emissions for SO ₂ , OC, BC; climatological SST
NUDGE	as CLIM; nudged meteorology; AMIP SST
GFAS	as NUDGE, using GFAS biomass burning emissions multiplied by factor 3.4

ues to the times and locations of the measurements at the locations of the respective AERONET stations (see Fig. 1). The retrieved AEs derived from the extinction measurements at 440 and 870 nm wavelengths are compared to collocated modeled values that are computed from simulated AOTs at 550 and 865 nm. Single-scattering albedos are taken from the L2 AERONET inversion product (Dubovik and King, 2000; Holben et al., 2006).

The global distribution of modeled AOT is additionally compared with retrievals from the MODerate-resolution Imaging Spectroradiometer (MODIS) instrument on the Aqua satellite (King et al., 1999). We used a data product based on Dark Target retrievals, developed by the NRL (Naval Research Laboratory) (Zhang and Reid, 2006; Hyer et al., 2011; Shi et al., 2011). For a direct comparison of model results and satellite retrievals the model AOTs were linearly interpolated to the time and location of available satellite observations (Schutgens et al., 2017).

4.2 Aerosol particle size

Aerosol size distributions were compared with in situ measurements from several stations described by Asmi et al. (2011a) for the year 2009 and with compiled number size distributions for the Aitken and accumulation modes compiled for different marine regions by Heintzenberg et al. (2000). For the European Supersites for Atmospheric Aerosol Research (EUSAAR; <http://www.eusaar.net/>, last access: 1 March 2019), particle number concentrations and size distributions in the size range between 30 and 500 nm dry diameter are available for total 24 stations. Here comparisons are done for 15 stations in different European regions (Fig. 2). The observations of number concentrations at the individual sites are converted into lognormal distributions, which facilitates comparisons of size distributions from the model that are computed as lognormal modes. Heintzenberg et al. (2000) compiled observations from 30 years of marine aerosol measurements and made them available on a 15° × 15° grid that is well suited for comparisons with global aerosol models. Measured number size distributions for the Aitken and accumulation modes are available. Since these observations were taken before the simulation period, they are used to evaluate the climatological median of the modeled size distribution.

4.3 In situ surface observations of aerosol species concentration

To evaluate the simulated aerosol mass mixing ratios at the surface, we compared the simulated data against those measured by the European Monitoring and Evaluation Program (EMEP; <http://www.emep.int>, last access: 1 March 2019) and the United States Interagency Monitoring of Protected Visual Environment (IMPROVE; <http://vista.cira.colostate.edu/improve/>, last access: 1 March 2019). Both of these observation networks provide data for the mass concentrations of individual chemical components. It should be noted that for surface stations in elevated regions the coarse model resolution of topographic features may make comparisons between surface measurements and simulation results inaccurate. From the EMEP and IMPROVE monitoring sites we compare the PM₁₀ aerosol mass concentration measurements for sulfate and black carbon. Additionally, for IMPROVE sites we compare organic carbon concentrations. In total, data from 530 stations are available for the EMEP and the IMPROVE networks; see Fig. 2. Comparisons of surface concentrations of BC and sulfate and EMEP observations were done for the period 2003–2012. Surface mass concentrations of OC were compared against IMPROVE observations for 2003 and 2004. For comparison the simulated concentrations at the model layer that corresponds to the altitude of the station of the compared species were sampled for the days when observations were available at each station and averaged in the same way as the observations. Moreover, the simulated concentrations are collocated to the locations of the individual stations.

Surface mass concentrations of mineral dust and sea salt aerosols were obtained from the AtmosphERre–Ocean Chemistry Experiment (AEROCE) (Arimoto et al., 1995) and the SEa/AiR EXchange program (SEAREX) (Prospero et al., 1989). Monthly surface mass concentrations are available for 29 sites that are used to evaluate modeled dust and sea salt concentrations. These observations have been extensively used for evaluating dust model results; see, e.g., Huneeus et al. (2011). The observation period for these stations was earlier than the simulation period, so we compare the 10-year average of monthly mean concentrations for the years 2003 to 2012.

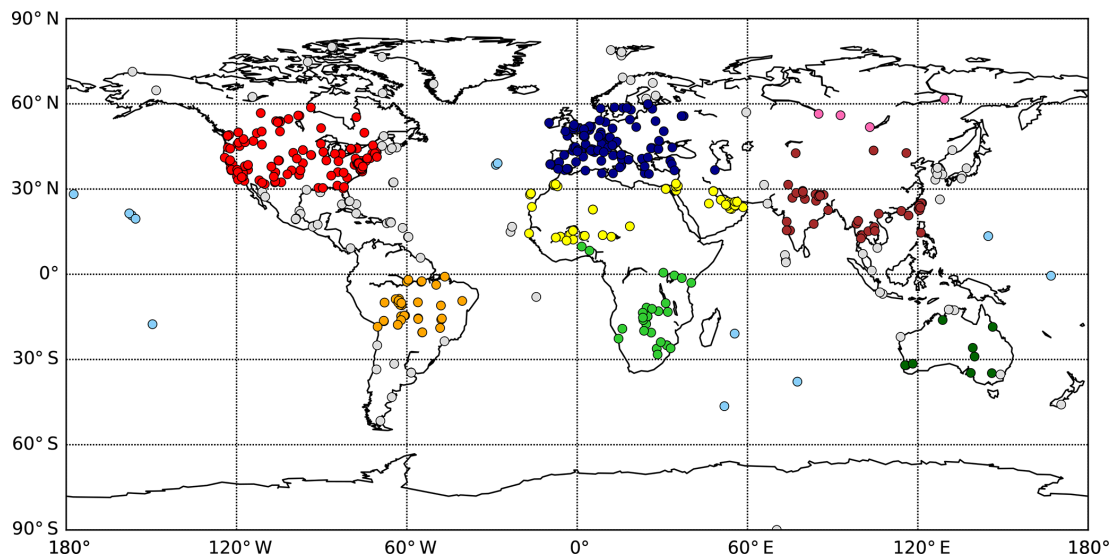


Figure 1. Locations of AERONET stations used for model evaluation. All stations are color coded according to the region to which they belong. Red: North America; dark blue: Europe; brown: East Asia; pink: Siberia; yellow: North Africa; green: South Africa; orange: South America; dark green: Australia; light blue: oceanic regions; grey: elsewhere (coastal and mixed).

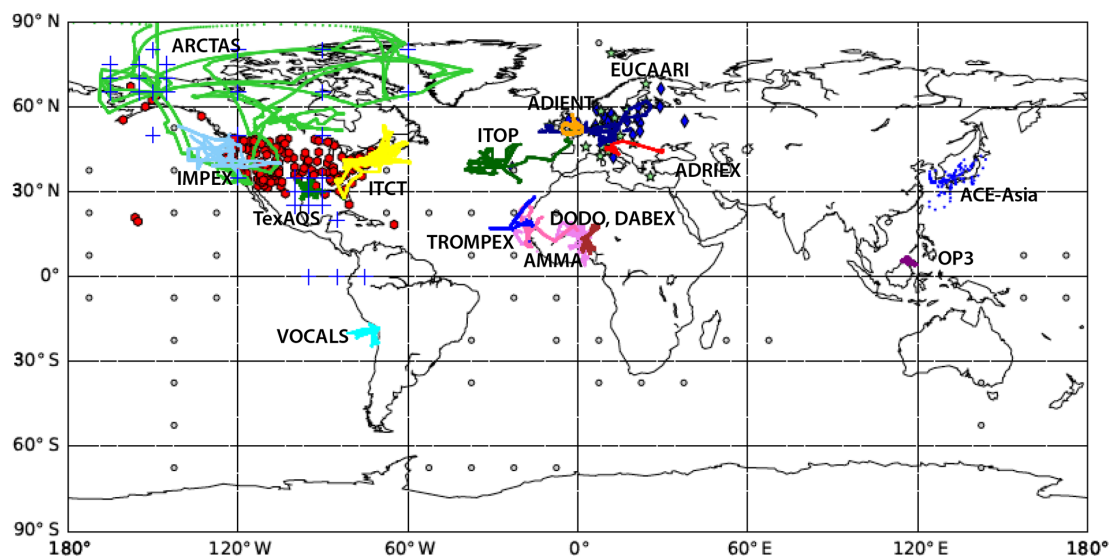


Figure 2. Networks of surface stations and research aircraft flight tracks used for model evaluation. Blue diamonds: EMEP stations with sulfate concentrations; red hexagons: IMPROVE stations with concentrations of sulfate, BC, and OC. Continuous color lines: aircraft flights for the evaluation of sulfate and OC vertical profiles (as described in Fig. 1 in Heald et al., 2011); blue crosses: regions for the evaluation of BC vertical profiles (Koch et al., 2009). Green stars: European sites with size distributions (Asmi et al., 2011a); grey circles: oceanic regions with size distributions (Heintzenberg et al., 2000).

4.4 Aircraft campaigns

Vertical profiles of simulated BC, OC, and SO_4 concentrations are compared to data from multiple aircraft campaigns. In Koch et al. (2009) aircraft campaign data for BC are compiled, which provide BC mass concentrations measured by single-particle soot photometers. Mass concentrations of sulfate and OC measured, e.g., by aerosol mass spectrometry or

filter measurements were compiled by Heald et al. (2011). The locations of the campaigns are shown in Fig. 2. Compared are the model concentrations in the grid cells that are crossed by the flight routes of the aircrafts for months when the measurements were taken (Watson-Parris et al., 2018).

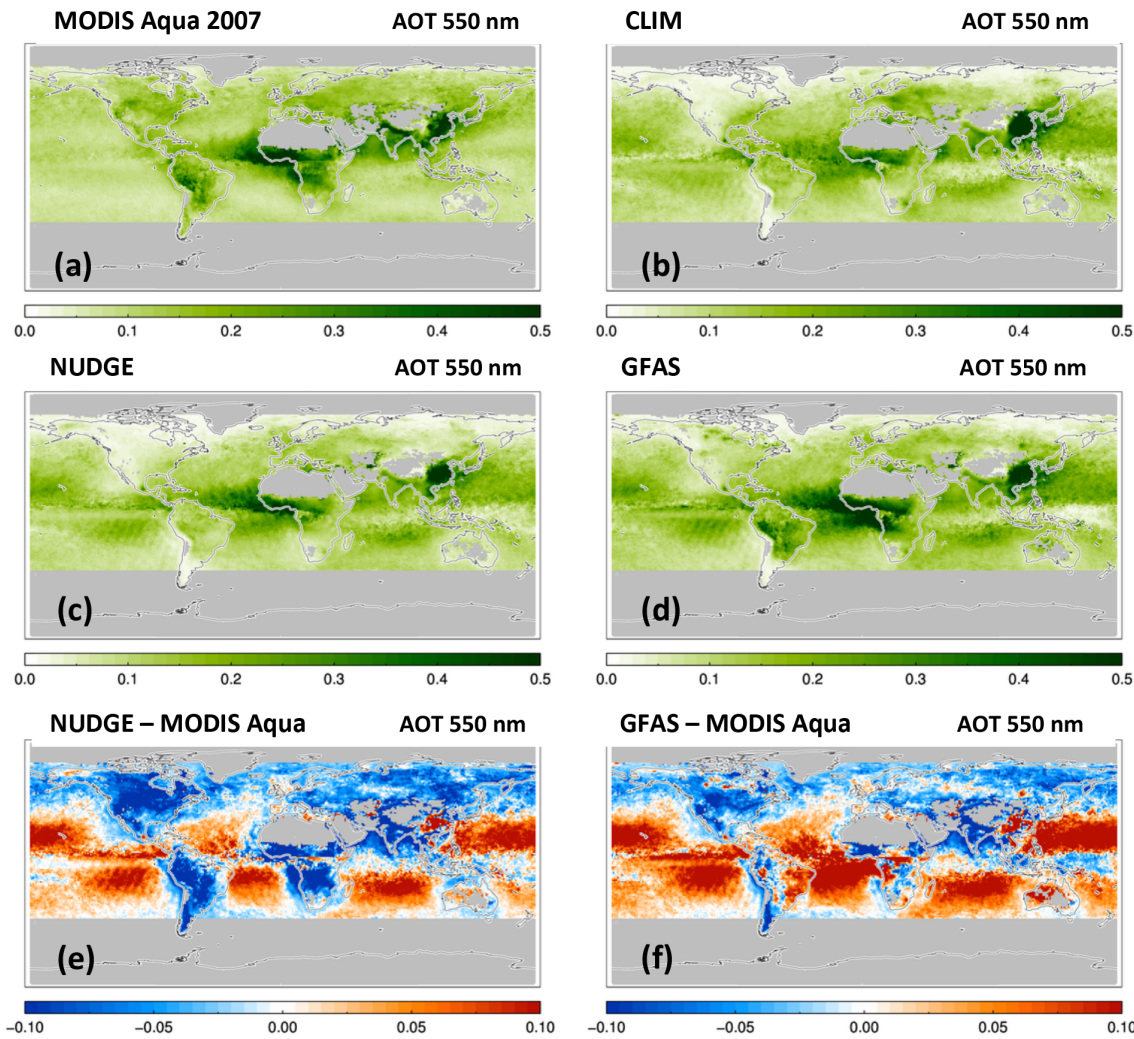


Figure 3. Comparison of annual average aerosol optical thickness (AOT) retrieved from MODIS Aqua satellite measurements (**a**) and for the experiments CLIM, NUDGE, and GFAS (**b–d**) for the year 2007. Additionally, differences between the simulated annual average of collocated AOT and the MODIS retrievals are given for the CLIM (**e**) and NUDGE (**f**) model results.

5 Results

5.1 Global distribution

For a general overview of the performance of the ECHAM6.3–HAM2.3 aerosol simulation, the simulated global AOT distributions for the CLIM, NUDGE, and GFAS experiments are compared with collocated retrievals from the MODIS Aqua satellite instrument for the example year 2007 (Fig. 3). The main features of the simulated AOTs agree overall with the observed patterns. However, while over land the MODIS comparisons point towards lower AOTs in the model results compared to the satellite retrievals, the model AOTs are overestimated over parts of the tropical and Southern Hemisphere oceans. Typical maximum concentrations downwind of the Sahara and the Sahel are caused by dust and biomass burning aerosol. Maximum AOTs in eastern Asia

result from anthropogenic aerosol sources. The shape of the aerosol plume over the Atlantic originating from the African continent is better matched in the NUDGE than in the CLIM results due to the more realistic large-scale wind fields responsible for long-range aerosol transport in the nudged simulation. For the GFAS results the AOT over the biomass burning regions is better matched in South America compared to the NUDGE results in which AOTs are underestimated, but overestimated in the eastern tropical Atlantic. The difference plots between the model results for the NUDGE and GFAS simulations and MODIS AOT highlight the fact that the model overestimates AOT in the tropical and subtropical ocean regions by more than 0.1, particularly for the GFAS results. A possible reason for this overestimation could be too-high concentrations of marine aerosol caused by too-high sea salt emissions in this region. Other causes for overestimating AOT in this region may originate from

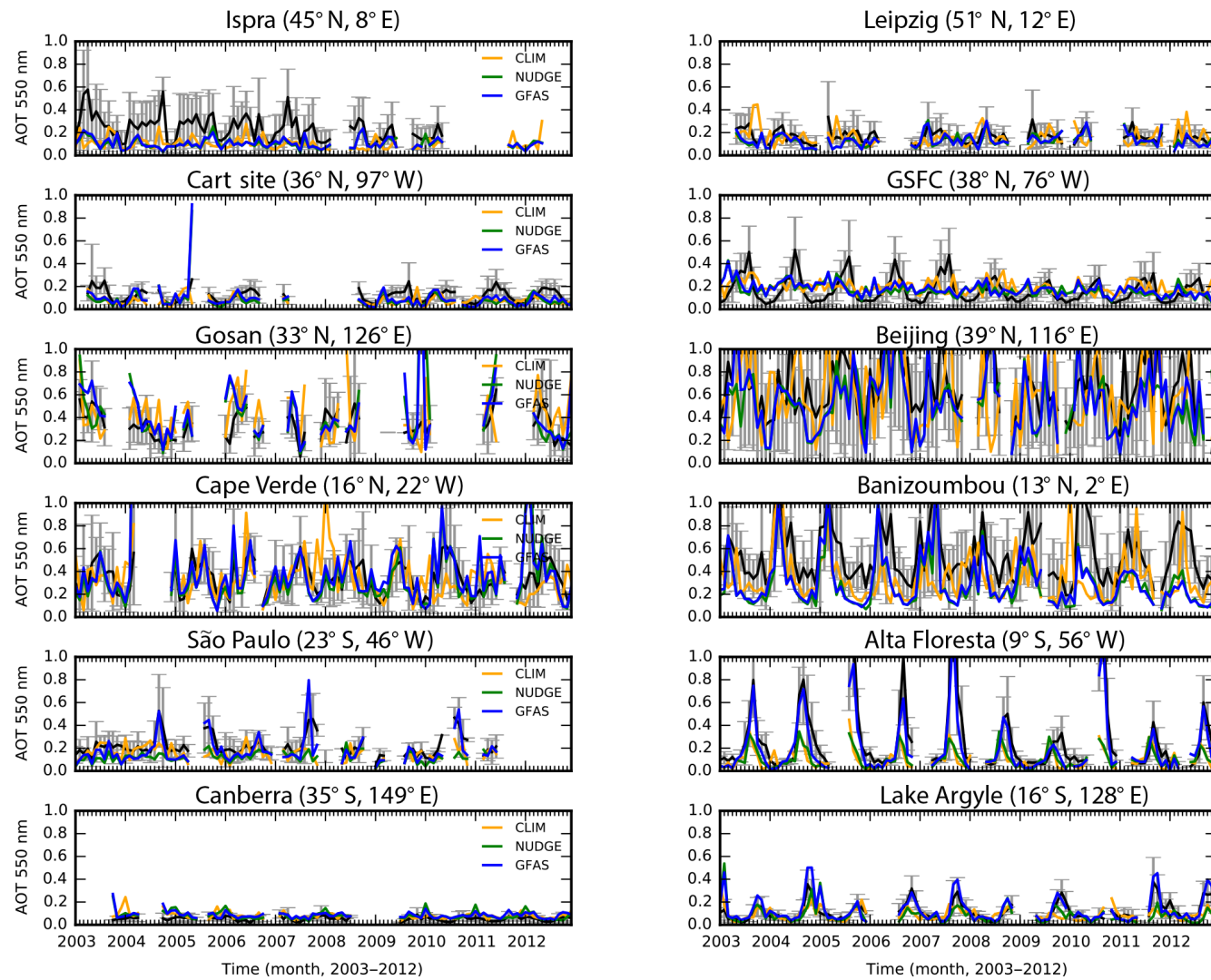


Figure 4. Time series (monthly means) of observed and simulated AOT (black line) from January 2003 to December 2012 at selected AERONET stations. Simulated monthly means were constructed from the daily mean outputs sampled on the same days of the observations and collocated to the observation position. Error bars show the standard variations due to daily variabilities in the measurements. Compared are model results for the CLIM (orange), NUDGE (green), and GFAS (blue) simulations.

too-high aerosol hygroscopic growth (as the model does not use a limitation of particle growth at high relative humidities) or too-low aerosol removal by wet deposition, which would have a noticeable effect in this region. Both simulations show too-low AOT in North America compared to the measurements, and AOT is lower by more than 0.1 compared to the observations. This may point to missing aerosol species in the model such as ammonium nitrate, which may contribute more than half of anthropogenic North American PM_{2.5} (Bauer et al., 2016; Croft et al., 2016). Other possible explanations are too-low OC emissions from combustion sources, secondary organic aerosol species in this region, or too-low hygroscopic particle growth.

5.2 Aerosol optical thicknesses, Ångstrom exponents, and single-scattering albedo at AERONET stations

The modeled AOTs and AEs are directly compared with collocated observations by the AERONET sun photometer stations mapped in Fig. 1 based on daily cloud-screened retrievals. Time series of simulated and observed AOTs (Fig. 4) shown for selected AERONET stations are monthly averages selected for days when observations were available. These stations where chosen for typical locations in Europe (Ispra, Italy, and Leipzig, Germany), Asia (Beijing, China, and Gosan, Korea), North America (the Cart site and GSFC, USA), South America (Alta Floresta and São Paulo, Brazil), Africa (Cape Verde, Banizoumbou, Niger), and Australia (Canberra, Lake Argyle). The magnitudes and temporal vari-

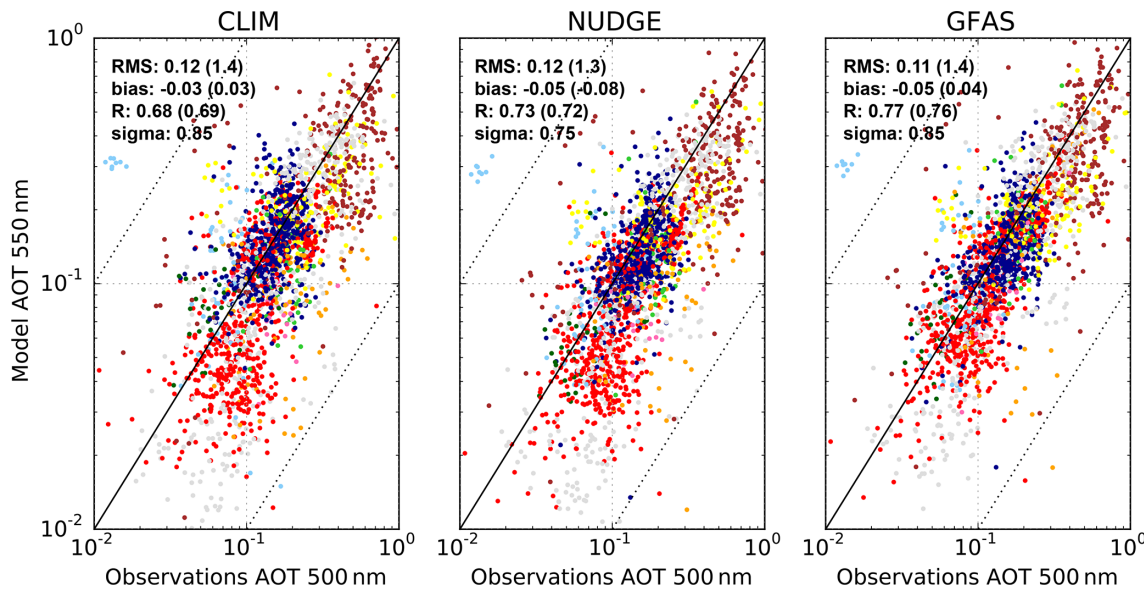


Figure 5. Scatterplots of observed versus simulated mean AOT over the period January 2003 to December 2012 at the AERONET stations shown in Fig. 1. The simulated yearly means are constructed by sampling the model from daily mean outputs for the same days of observations and collocated to the locations of the observations. Stations are color coded depending on the regions to which they belong as shown in Fig. 1. Red: North America; dark blue: Europe; brown: East Asia; pink: Siberia; yellow: North Africa; green: South Africa; orange: South America; dark green: Australia; light blue: oceanic regions; grey: elsewhere (coastal and/or mixed). Compared are model results for the simulations described in Sect. 2.3. For each comparison the root mean square error (RMS; with normalized RMS in parentheses), the Pearson correlation coefficient (R , shown on log scale in parentheses), the absolute bias (normalized bias), and the ratio between simulated and observed standard deviation (sigma) are given.

ations in AOT for the NUDGE, CLIM, and GFAS simulations are mostly well matched with the observations. Seasonal and interannual variabilities are generally well reproduced in the model. The better match of the results from the nudged simulations compared to CLIM for stations largely impacted by long-range-transported aerosol, such as Cape Verde, is evident. At stations where aerosols from biomass burning contribute significantly to AOT, differences between NUDGE and GFAS results are also clearly evident (Alta Floresta, São Paulo). For GFAS the individual AOT maxima and year-to-year differences are better matched with the observations compared to the CLIM and NUDGE results due to biomass burning emissions based on actual satellite retrievals. In contrast, projected values of the ACCMIP emissions are used in the NUDGE and CLIM experiments. While for the CLIM simulation the individual AOT maxima are less well matched compared to the NUDGE simulation, the seasonal changes are generally in reasonable agreement with the observations, indicating the important role of the seasonality of emissions and atmospheric processes in addition to the accurate transport patterns. While at most stations the magnitude of the AOTs are well matched between the model and observations, there are some exceptions: e.g., at the Ispra site in northern Italy all model results underestimate the measurements by about a factor of 2, and at the station GSFC in Maryland, USA, the observed seasonal cycle is not repro-

duced. The underestimation of AOT in the model at the location of Ispra may be explained by a misrepresentation of the topography at the location near the foothills of the Alps and thus the atmospheric flows. Otherwise, even in highly polluted urban locations such as Beijing the model results and observations are well matched in terms of magnitude and temporal variations at monthly and interannual timescales. The same is the case for locations with very low AOT (Canberra).

In addition, the model results are also provided as scatterplots (Fig. 5). The values are selected for days when measurements were available and then averaged for the respective year. Almost all annual AOT averages are well within 1 order of magnitude of the observations. The Pearson correlation coefficient for AERONET AOTs is 0.73 for NUDGE, 0.77 for GFAS, and 0.68 for CLIM results. The average normalized (by the mean value) root mean square error is 1.3 for the NUDGE results, slightly better than for CLIM with 1.4. The model results have a slight negative bias of -0.03 (CLIM) and -0.05 (NUDGE, GFAS). The ratio of standard deviation for the model and observations is between 0.75 (NUDGE) and 0.85 (CLIM, GFAS), indicating lower variability in the model results compared to the observations. That the GFAS simulation compares better to the observations than the NUDGE results reflects the role of the annually varying emissions from biomass fires based on satellite data

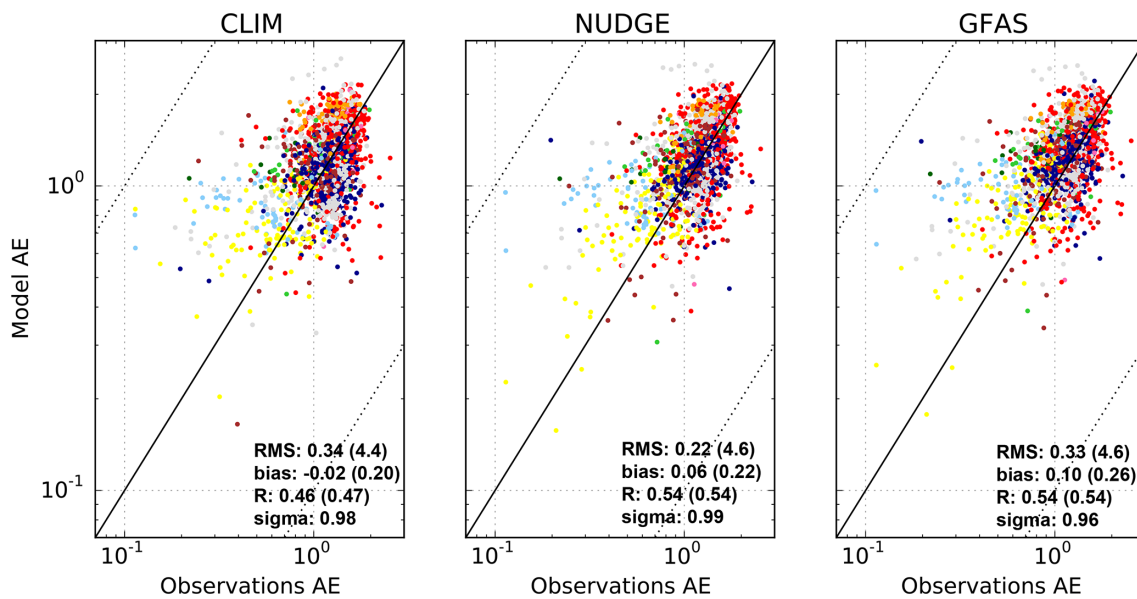


Figure 6. Scatterplot of observed versus simulated mean Ångstrom exponents over the period January 2003 to December 2012 at the AERONET stations shown in Fig. 1 for the CLIM, NUDGE, and GFAS simulations. The color coding of the results is as in Fig. 5, and the simulated means and statistical parameters are constructed and calculated, respectively, as in Fig. 5.

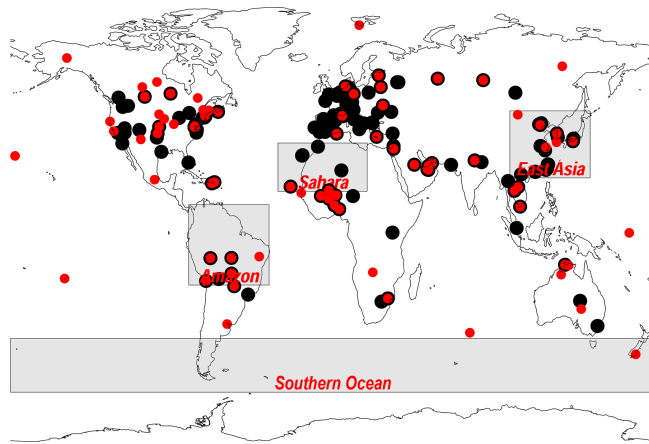


Figure 7. AERONET stations and regions used in the monthly summaries for AOT, AE (direct sun measurements, red symbols), and SSA (version 2 inversion product, black symbols; Holben et al., 2006) for 2007 in Fig. 8. The stations for the AOT and AE summaries are selected as being regionally representative, as in Kinne et al. (2013).

in GFAS. In particular, in the GFAS simulation the agreement is better for North and South America for locations that have annual average AOT values lower than 0.1, whereas the ACCMIP emission scenario used in the NUDGE experiment leads to too-low AOTs in the model.

The simulated Ångstrom exponents giving an indication of effective aerosol particle sizes in the atmospheric columns are also compared with the AERONET data (Fig. 6). The correlation of the observed and simulated AE of 0.46–0.54

for the results is lower than the correlation for AOT. It can be expected that modal schemes such as HAM better simulate mass mixing ratios as size distributions of aerosols. Root mean square errors of about 0.2–0.3 are similar for all model results. Compared to the observations, the simulated values have a positive bias, particularly in North Africa, South America, and oceanic regions, which means that the simulated particle sizes are too small. The bias in regions that are dominated by dust and sea salt aerosol reflects the fact that natural coarse-mode aerosol particles may not be well represented in the modal aerosol scheme. The AE values in the GFAS simulation have a slightly higher positive bias (0.1) compared to the NUDGE simulation (0.06). The positive AE bias in South America where the aerosol load is strongly impacted by biomass burning aerosols could be an indication that biomass burning aerosols may contain more coarse-mode aerosol than assumed in the model. For the AE values at North American sites (red symbols) the AE values vary more strongly in the model than in the observations in all experiments, which is not the case for the AOTs. Other than possible contributions of secondary organics, which may be misrepresented in this model setup, this bias may also be caused by sporadic dust events in this region that are not simulated in the model, but would lead to lower observed AEs at times of dust emissions. However, this would lead to higher dust variability in the observations than in the model, which is not found.

Annual cycles of AOT, AE, and SSA are shown for averaged results for the AERONET stations indicated in Fig. 7 and four regions (East Asia, Amazon, Sahara, Southern Ocean) in Fig. 8. AOT model results for NUDGE,

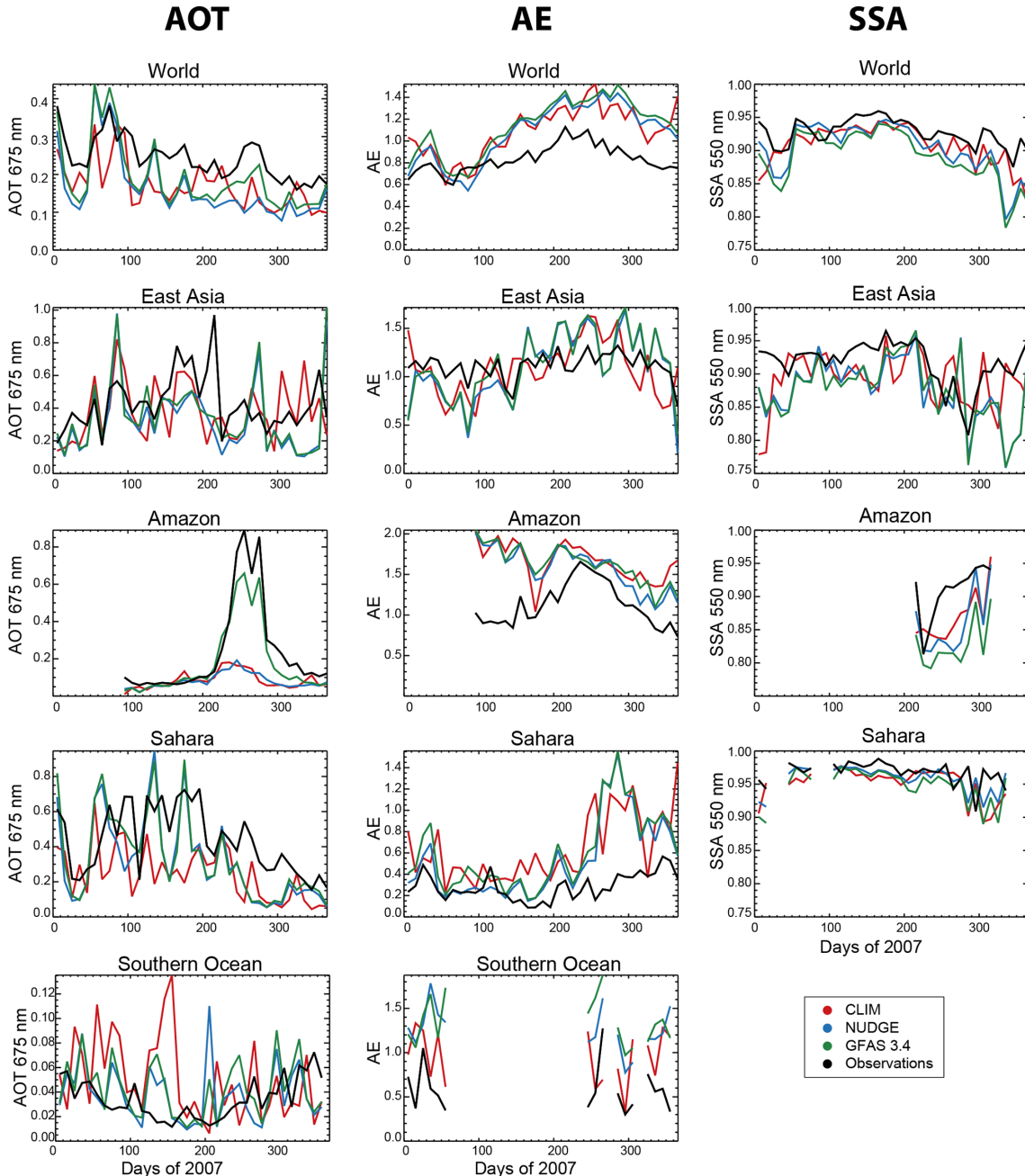


Figure 8. Annual cycle of AOT (left panels), AE (middle panels), and SSA (right panels) from AERONET retrievals as global averages and summarized for several regions (the world, East Asia, Amazon, the Sahara, and the Southern Ocean) as shown in Fig. 7 for the year 2007.

GFAS, and CLIM are compared to AERONET direct sun retrievals at 675 nm, while SSA from the model is compared to the AERONET inversion product (Holben et al., 2006) at 550 nm. For AOT and AE the AERONET stations used for this comparison were selected as being regionally representative, as in Kinne et al. (2013). For the time series the individually collocated model data and observations were aggregated over regions and 10 days. In the global average the modeled AOT underestimates the observations by values of about 0.05

to 0.1 in the different simulations, with the best agreement in Northern Hemisphere (NH) spring months when AOT is highest. The seasonal AOT pattern is better matched for NUDGE and GFAS than for CLIM model results due to the more realistic transport patterns. The observed NH fall maximum is due to aerosol from biomass burning smoke in the Amazon region, which is matched by the GFAS results due to the realistic seasonal distribution of biomass burning emissions in that simulation. The CLIM results underestimate

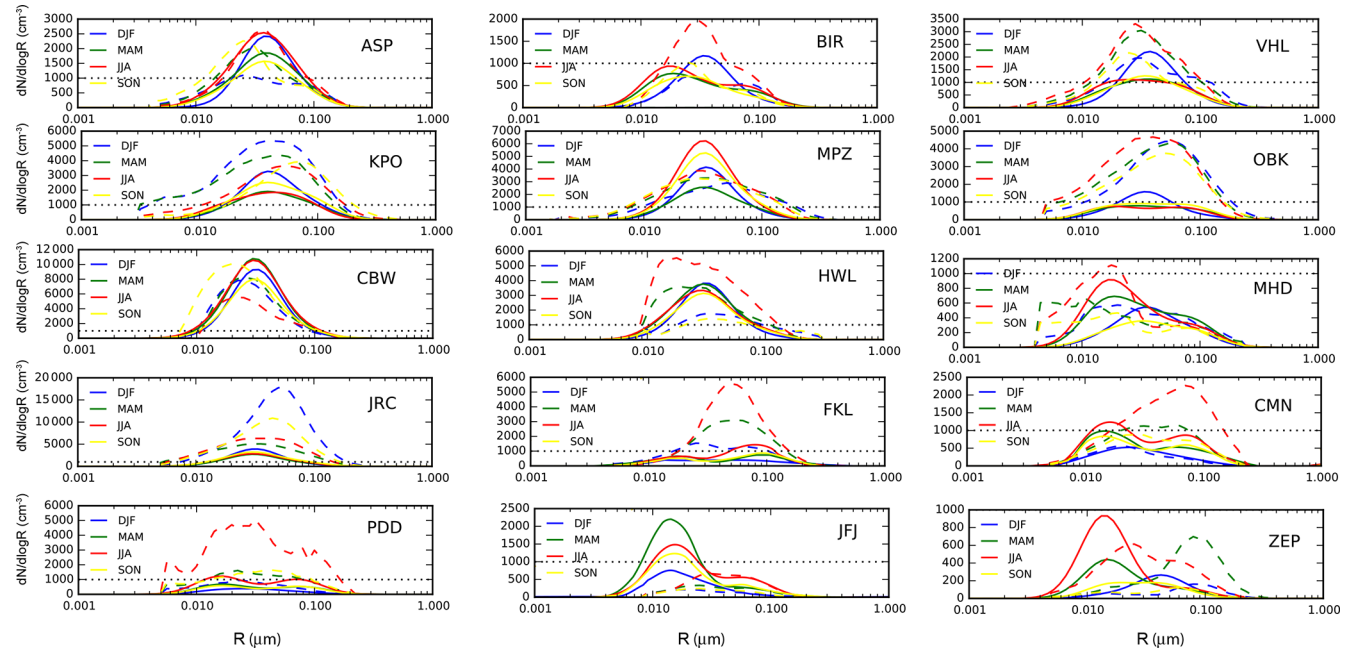


Figure 9. Observed (dashed lines) and simulated (solid lines) (NUDGE simulation) near-surface median aerosol size distributions for European field monitoring sites (EUSAAR) for 2009 (Asmi et al., 2011a). Data are for winter (blue), spring (green), summer (red), and fall (yellow). The simulated size distributions are the median of the number of daily mean size distributions per season. The top panels contain data for three Nordic and Baltic stations (ASP: Aspvreten; BIR: Birkenes; VHL: Vavihill), the second row contains central European sites (KPO: K.Puszta; MPZ: Melpitz; OBK: Košetice), and the third row western European stations (CBW: Cabauw; HWL: Harwell; MHD: Mace Head). The fourth row represents stations in Mediterranean countries (JRC: Ispra; FKL: Finokalia; CMN: Monte Cimone), and the fifth row represents high-altitude (PDD: Puy de Dôme; JFJ: Jungfraujoch) and Arctic (ZEP: Zeppelin) stations.

AOT in the Amazon in the NH fall season and the Sahara in all seasons except the winter months. Mineral dust aerosols dominate the aerosol composition in the Sahara region and are produced by strong surface winds. Here, the CLIM results clearly deviate from the results with the nudged model, which could also be seen in the daily results above. Except in East Asia where aerosol is dominantly anthropogenic, the AE model results are higher than the observations in agreement with the scatterplot in Fig. 6. Again this can be interpreted as the model underestimating the particle size for coarse-mode aerosol particles like mineral dust or sea salt. Specifically, the overestimation of AE in the Sahara in NH fall by the model, pointing to an underestimation in particle sizes, may be related to too-low Saharan dust emissions in this season, which is also indicated by too-low seasonal AOT compared to the observations in this region. Thus, the high AE is controlled by transported anthropogenic aerosol such as sulfate from anthropogenic fossil fuel or wood burning. Too-low dust emissions in this season may be related to underestimates of dust emission events caused by moist convection, which cannot be well represented by the parameterized convection in the model. The SSA links the aerosol properties resulting from particle size and composition to their absorption and thus their radiative effect (see also Neubauer et al., 2019). The model results lie slightly below the AERONET inversions

in all regions. In the global mean, the retrieved AERONET SSA values vary between 0.88 and 0.95, with values as high as 0.98 in the Sahara and as low as 0.8 during some months in the Amazon and East Asia due to high black carbon loads. In some instances the modeled SSAs fall below 0.8. The overall slightly lower modeled SSA compared to the AERONET inversions may result in a solar aerosol absorption that is biased high in the model results. On the other hand, the too-low particle size in coarse-mode mineral dust that is indicated by the overestimate of AE in mineral-dust-dominated regions could result in a too-high SSA in the model as supermicron dust particles are more absorbing and thus have lower SSA compared to submicron dust particles for the same complex refractive indices (Lacis and Mishchenko, 1995). This misrepresentation of particle sizes would thus result in an overall underestimate of aerosol absorption in the model.

5.3 Size distribution

Aerosol size distributions are compared for seasonal averages in the NUDGE simulation to observations at several EUSAAR stations (Asmi et al., 2011a) representing different European regions (Fig. 9). Only Aitken and accumulation modes were measured, and therefore only these modes are considered in the comparisons. Agreements of number

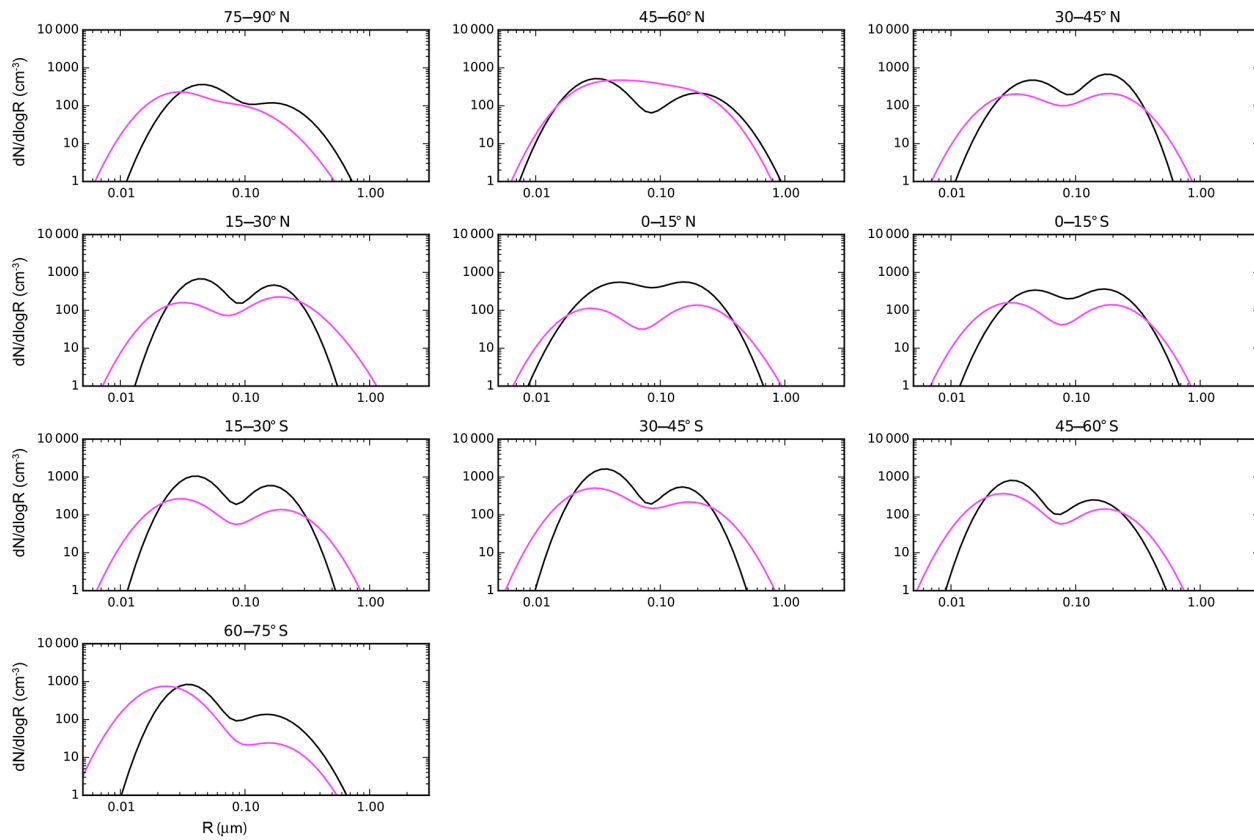


Figure 10. Size distribution of simulated (pink lines) and measured (black lines) aerosol number in the marine boundary layer for the NUDGE simulation. The observed size distribution corresponds to a 30-year climatology for the Aitken and accumulation modes (soluble and insoluble) (Heintzenberg et al., 2000). The simulated size distributions correspond to a 10-year annual average over the locations of the measurements and zonally averaged between the given latitude bounds.

concentrations, particle size distributions, and seasonal variations are evident for many of the stations, particularly notable at stations in the northern and western parts of Europe. In central Europe the number size concentrations are underestimated at the stations K. Puszta and Košetice, and the same is the case for the station Ispra in northern Italy, particularly in the winter season. For Ispra this underestimate in number size concentrations is consistent with the underestimated AOTs in this location shown in Fig. 4. As mentioned above, this discrepancy may be due to insufficient resolution of the regional topography and thus too-strong mixing of air masses in this region. Also, the model underestimates the maximum number concentration at southern European stations in summer in Finokalia and Monte Cimone. In other seasons the agreement is better, at least at the latter location. At the high-altitude stations Puy de Dôme and Jungfraujoch some misrepresentations of maximum number size concentrations occur, whereby the concentrations are clearly overestimated in the summer months at Puy de Dôme, and the Aitken mode concentrations are overestimated at Jungfraujoch in the model compared to the observations. The same is the case at the high-latitude Zeppelin station. Overall the

agreement is good in most cases, considering that global model simulation results are compared to measurements at individual station locations that may not be representative for large areas (Schutgens et al., 2016).

For remote regions, particle number size distributions averaged for oceanic latitudinal bands as compiled by Heintzenberg et al. (2000) (Fig. 10) are compared to model results. In the marine regions the measurements generally show more separated Aitken and accumulation modes than at the locations of the EUSAAR measurements, which are close to aerosol source regions. This difference is the consequence of the presence of “aged” aerosol in these remote regions for which microphysical processes like coagulation and condensation have led to the development of well-defined aerosol modes. The model results show generally good agreement in terms of mode sizes and concentration maxima (note that here the y axes for the number concentration are logarithmic in contrast to the linear axes used in Fig. 9). Only comparisons for the NUDGE experiment are shown here. The comparisons for the CLIM and GFAS simulations give very similar results in terms of aerosol number size distributions. The shapes of the size distributions and maximum concen-

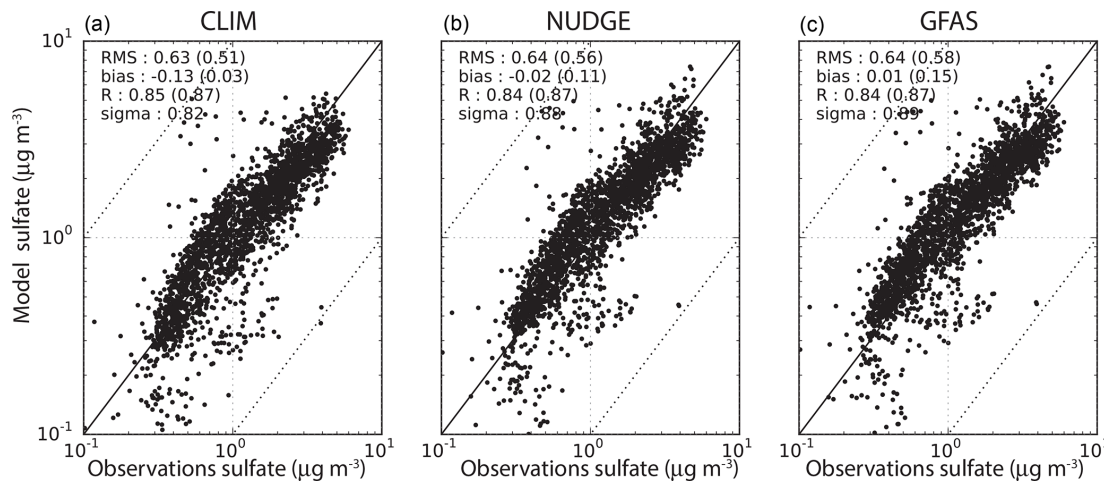


Figure 11. Scatterplot of sulfate surface concentrations from the EMEP and IMPROVE networks and from the CLIM (a), NUDGE (b), and GFAS (c) simulations. Model data were selected for days when observations were available at each station location and yearly averaged. Observed and collocated simulated averages for all available stations (see Fig. 2 for the location of the stations) were compared for the years 2003 to 2012 for IMPROVE and EMEP stations. For each comparison the root mean square error (RMS; with normalized RMS in parentheses), the correlation coefficient (R , shown on log scale in parentheses), the absolute bias (normalized bias), and the ratio between simulated and observed standard deviation (sigma) are given.

trations generally agree with observations, but the widths of the modes of size distributions are slightly larger for the model than the observations in many regions. Particularly, the size distribution for the Aitken mode is wider in the model than in the observations, which points to an overestimate of the width of the Aitken mode in the model by the prescribed mode standard deviation of 1.59. In the tropics, in particular for the region 0–15° N, the maximum number size concentrations are too low by nearly an order of magnitude in the model compared to the observations. At northern and southern high latitudes the number size distributions in the model are shifted to smaller sizes compared to the observations. However, the distribution at midlatitudes compare well considering that the time period of the observations and the model do not agree. For the latitude band between 45 and 60° S the maximum and width of the accumulation mode matched the observations better than the previous model version described in Zhang et al. (2012). This points to an improvement in the size distribution of marine aerosol, which has a large contribution to aerosol concentrations in the boundary layer at these latitudes. This will be further discussed in Sect. 5.7.

While the comparison of simulated AE with sun photometer measurements in Fig. 6 indicates a possible positive bias in the model, which hints towards too-small particle sizes in the model, this is in general not evident in this direct comparison of particle size distributions at the surface. However, since coarse-mode particles were not included in the size distribution measurements, the model's ability to realistically simulate coarse-mode particles, e.g., for mineral dust and sea salt, cannot be evaluated with these measurements. Alterna-

tively, hygroscopic particle growth or may be too low in the model.

5.4 Aerosol species

The global aerosol species budgets for burdens, emissions, sinks, and lifetimes for the CLIM, NUDGE, and GFAS experiments are summarized in Table 3. Here the burdens are also compared with the previous version ECHAM5–HAM2.0 (Zhang et al., 2012) and also with results from the AeroCom aerosol model intercomparison (Textor et al., 2006). All values of the budgets for the individual aerosol species that were computed with the model are within the range of the AeroCom values. While the values did not considerably change compared to the earlier version by Zhang et al. (2012) for the mostly anthropogenic species SO_4 , BC, and OC, differences for dust and sea salt emissions are evident. Dust emissions increased from about 900 to 1100 Mt yr^{-1} due to the regional tuning and are thus closer to the AeroCom average of 1800 Mt yr^{-1} . However, the magnitude of dust mass emission fluxes also depends on the size range considered in the dust emission calculation. Particle sizes exceeding several micrometers can cause high emission fluxes but do not considerably contribute to atmospheric burdens due to their fast sedimentation rates. Due to slightly increased atmospheric lifetimes in the current model version, global and annually averaged dust burdens increased from 11 to about 17 Tg, also in agreement with the AeroCom average burden of 19.2 Tg. Sea salt mass emissions were considerably reduced by more than a factor of 4 with the new emission parameterization compared to the earlier version, and as a consequence deposition fluxes and atmospheric bur-

Table 3. Comparison of global annual aerosol budgets. Compared are the results from ECHAM6.3–HAM2.3 with the earlier version ECHAM5–HAM2.0 as described in Zhang et al. (2012) (Table 8 therein) and the simulations CLIM, NUDGE, and GFAS averaged over the years 2003–2012. The results are also compared with the multi-model AeroCom results by Textor et al. (2006).

	ECHAM5–HAM2.0		ECHAM6.3–HAM2.3		AeroCom
	Zhang et al. (2012)	CLIM	NUDGE	GFAS	Textor et al. (2006)
Sulfate					
Burden (Tg S)	0.85	0.74	0.78	0.81	0.67 (25 %)
Sources (Tg S yr ⁻¹)					
Emissions + production	70.9	73	73	74	59.7 (22 %)
Sinks (Tg S yr ⁻¹)					
Sedimentation	1.56	0.70	0.72	0.71	
Dry deposition	2.33	2.08	2.11	2.15	6.9* (55 %)
Wet deposition	66.6	69.9	69.4	71.0	53.0 (22 %)
Lifetime (days)	4.4	3.7	4.0	4.0	4.1 (18 %)
BC					
Burden (Tg)	0.13	0.14	0.14	0.26	0.24 (42 %)
Sources (Tg yr ⁻¹)					
Emissions	7.7	8.1	8.1	12.5	11.9 (23 %)
Sinks (Tg yr ⁻¹)					
Sedimentation	0.02	0.02	0.02	0.03	
Dry deposition	0.64	0.71	0.74	0.93	2.6* (55 %)
Wet deposition	7.1	7.4	7.5	11.6	9.4 (31 %)
Lifetime (days)	5.9	6.3	6.5	7.5	7.1 (33 %)
OC					
Burden (Tg)	1.5	1.0	1.0	2.2	1.7 (27 %)
Sources (Tg yr ⁻¹)					
Emissions	68	69.0	69.0	123.0	97.0 (26 %)
Sinks (Tg yr ⁻¹)					
Sedimentation	0.19	0.18	0.19	0.32	
Dry deposition	4.5	5.4	5.6	7.5	19.2* (49 %)
Wet deposition	60.3	64.4	64.4	116.	76.7 (32 %)
Lifetime (days)	8.4	5.4	5.5	6.6	6.5 (27 %)
Dust					
Burden (Tg)	11.6	16.5	17.9	17.3	19.2 (40 %)
Sources (Tg yr ⁻¹)					
Emissions	805	1124	1145	1107	1840 (49 %)
Sinks (Tg yr ⁻¹)					
Sedimentation	341	370	387	378	
Dry deposition	56.0	77.0	70.0	68.0	1235* (84 %)
Wet deposition	410	687	696	669	607 (54 %)
Lifetime (days)	5.4	5.3	5.7	5.7	4.1 (43 %)
Sea salt					
Burden (Tg)	11.6	3.9	3.9	3.9	6.4 (54 %)
Sources (Tg yr ⁻¹)					
Emissions	6110	1212	1101	1092	6280 (199 %)
Sinks (Tg yr ⁻¹)					
Sedimentation	2038	255	244	243	
Dry deposition	1484	98	82	81	4377* (219 %)
Wet deposition	2591	863	778	770	1902 (77 %)
Lifetime (days)	0.69	1.2	1.3	1.3	0.41 (58 %)

* For the AeroCom results dry deposition also contains the sedimentation fluxes due to gravitational settling. The numbers in parentheses for the AeroCom results show the standard deviations of the AeroCom results as a measure of model diversities.

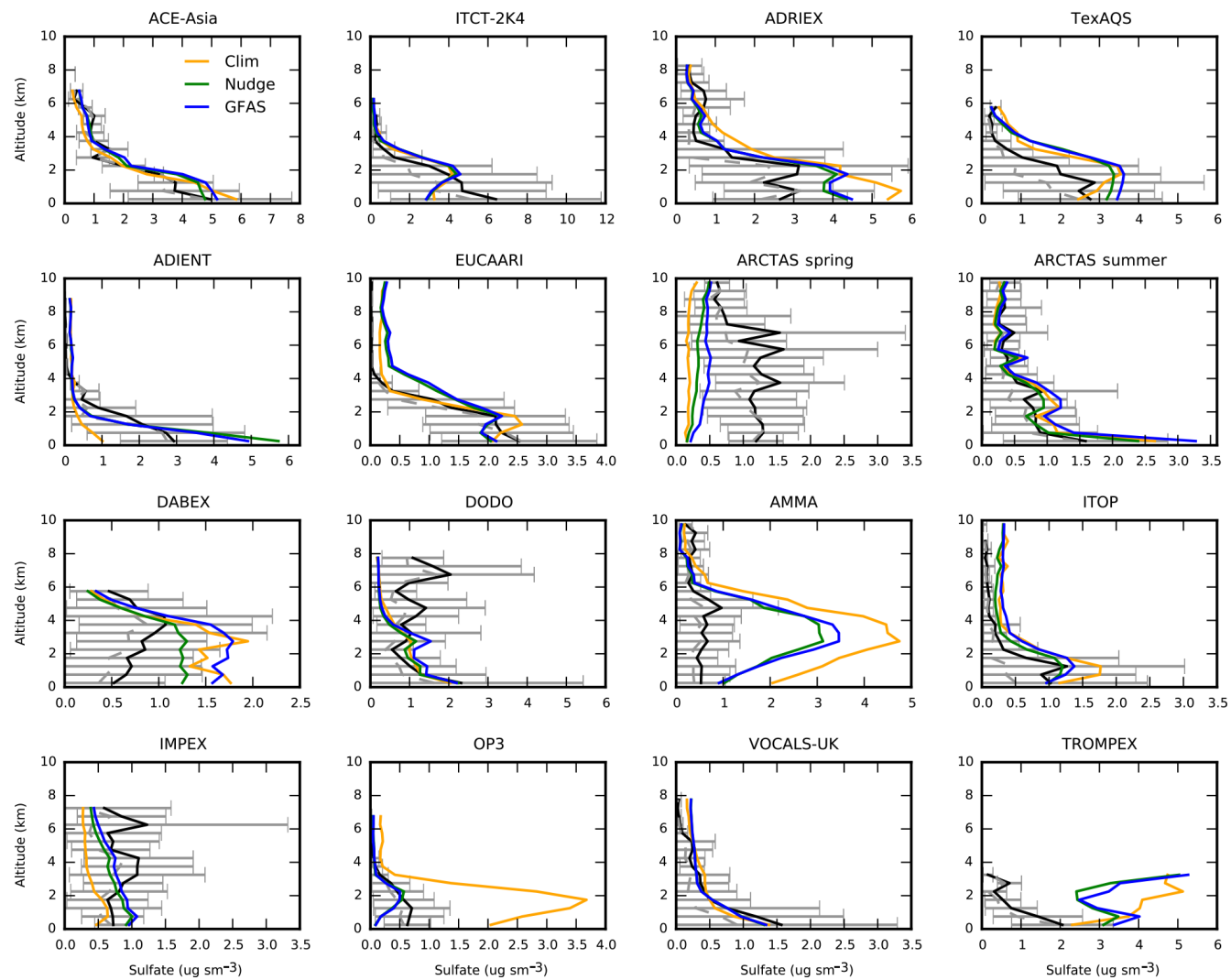


Figure 12. Vertical profiles of observed concentrations of sulfate (black) and simulated concentrations from the three simulations: CLIM (orange), NUDGE (green), and GFAS (blue). The observations are provided for 16 aircraft campaigns that investigated different regions of the world from 2001 to 2009 (Heald et al., 2011) (see also Fig. 2). The model is sampled along the flight tracks using a temporal average of the outputs over the duration of the campaign, and the error bars show the variabilities in the measurements. Simulated vertical profiles are shown as monthly and regional averages.

dens of sea salt aerosol were also reduced. The atmospheric sea salt burden is reduced by a factor of about 2–3, which is less than the reduction in emissions. This is consistent with the nearly doubled atmospheric lifetimes of sea salt particles compared to the earlier model version, which is a consequence of the smaller particle sizes in the new parameterization, ignoring the super-coarse sea salt fraction, which deposits very quickly.

5.5 Comparison of sulfate, OC, and BC with observations

The locations of the EMEP and IMPROVE stations as well as the flight patterns of the research flights used for comparisons

of model results and measurements for the species SO_4 , OC, and BC are shown in Fig. 2.

5.5.1 Sulfate

The comparison of sulfate aerosols with surface concentration measurements at EMEP and IMPROVE stations (Fig. 11) shows that the different simulations agree similarly well with the observations for the three experiments. The statistical values given in each panel are the root mean square error (RMS; with normalized RMS in parentheses), the absolute bias (normalized bias), R (correlation coefficient; on log scale, correlating logarithms of concentration that emphasize variations in concentration over large distances from

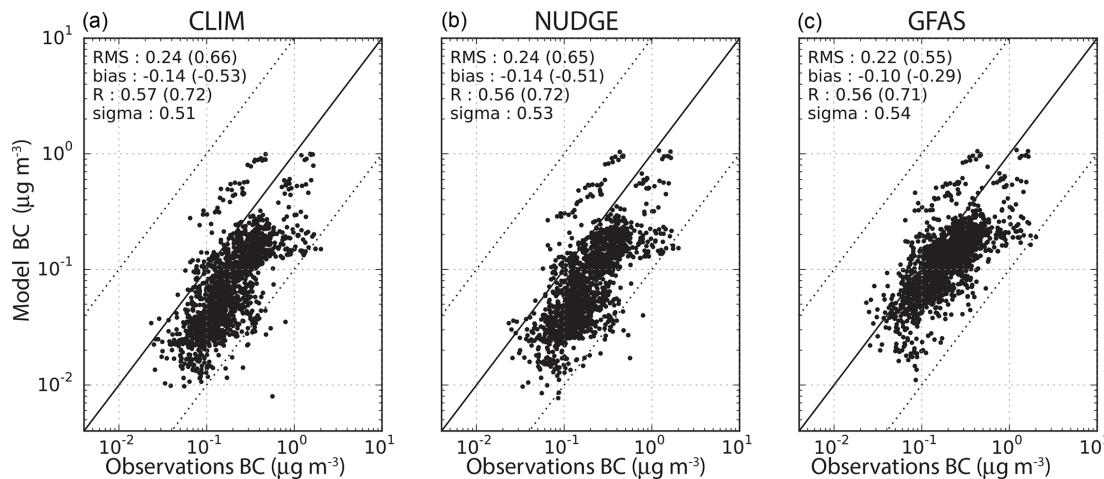


Figure 13. As Fig. 11 for black carbon (BC) aerosol.

the source), and sigma (the ratio between simulated and observed standard deviations). For all experiments the correlation coefficients between modeled and measured surface concentrations are 0.84–0.85 for the comparison at EMEP and IMPROVE stations, showing that simulated surface concentrations of sulfate aerosol are not affected by different biomass burning emissions in these locations. Also, for the secondary sulfate particles the use of nudged meteorology does not significantly improve the distribution of the simulated particles compared to the free simulation CLIM. The biases of the averaged model results compared to the observations are low.

The comparisons to aircraft measurements (Fig. 12) are mostly within the error bars for the observations in the figure that indicate the measurement variabilities. In particular, reasonable agreement is found in the free troposphere within the different experiments and comparisons with observations. In the Sahel region the results for the AMMA campaign show 4–5-fold overestimates in sulfate concentrations at heights between 2 and 4 km compared to the measurements, which may be related to low dry deposition velocities of SO_2 over bare soils. While the NUDGE and GFAS results are mostly in close agreement, as emissions of the sulfate precursor SO_2 from biomass burning are generally low compared to anthropogenic emissions, the results from the CLIM simulations deviate considerably from the other results, e.g., for the AMMA and OP3 campaigns, indicating that for vertical distribution the use of realistic wind speeds and directions to simulate aerosol transport is important when evaluating SO_4^{2-} concentrations with aircraft measurements.

5.5.2 Black carbon

As for sulfate, the simulated BC aerosol concentrations are compared to in situ measurements by EMEP and IMPROVE in Europe and North America (Fig. 13). There is a negative

bias in the model simulation compared to the observations, which is reduced in the GFAS experiment. The correlations (R values between 0.54 and 0.57) are lower than for sulfate. Particularly for concentrations lower than $0.5 \mu\text{g m}^{-3}$, the model underestimates the observed surface concentrations, which may be caused by too-low local emissions or too-fast removal of the particles.

The comparisons to aircraft data for BC use the same observations as the BC AeroCom model intercomparison study by Koch et al. (2009). For flights at low latitudes and mid-latitudes (AVE Houston, CR-AVE, TC4, CARB) the model overestimates the BC concentrations in the free troposphere in most cases, which may be due to either too-strong vertical transport or too-low removal above the boundary layer. Similar overestimates were found for most models compared by Koch et al. (2009). For the flights at high latitudes (ARCTAS, ARCPAC) the GFAS simulations agree well with the observations. In the CLIM and NUDGE results BC concentrations in the boundary layer are lower, but remain in the range of uncertainty of the measurements. Above 200 hPa of altitude the modeled BC concentrations remain quite constant for all simulations. Since in the compared aircraft studies no measurements were taken at those high altitudes it is not clear if the modeled BC distribution at high altitudes is realistic.

5.5.3 Organic carbon

The comparisons of OC concentrations with in situ measurements are similar to the evaluation of SO_4^{2-} and BC concentrations except that OC measurements were not available for EMEP stations. The comparison of surface concentration measurements at the IMPROVE stations (Fig. 15) shows a negative bias, which may be a consequence of neglecting to explicitly compute the formation of secondary organic aerosols in this model setup or missing OC sources, such as marine emissions of organic species. However, since the

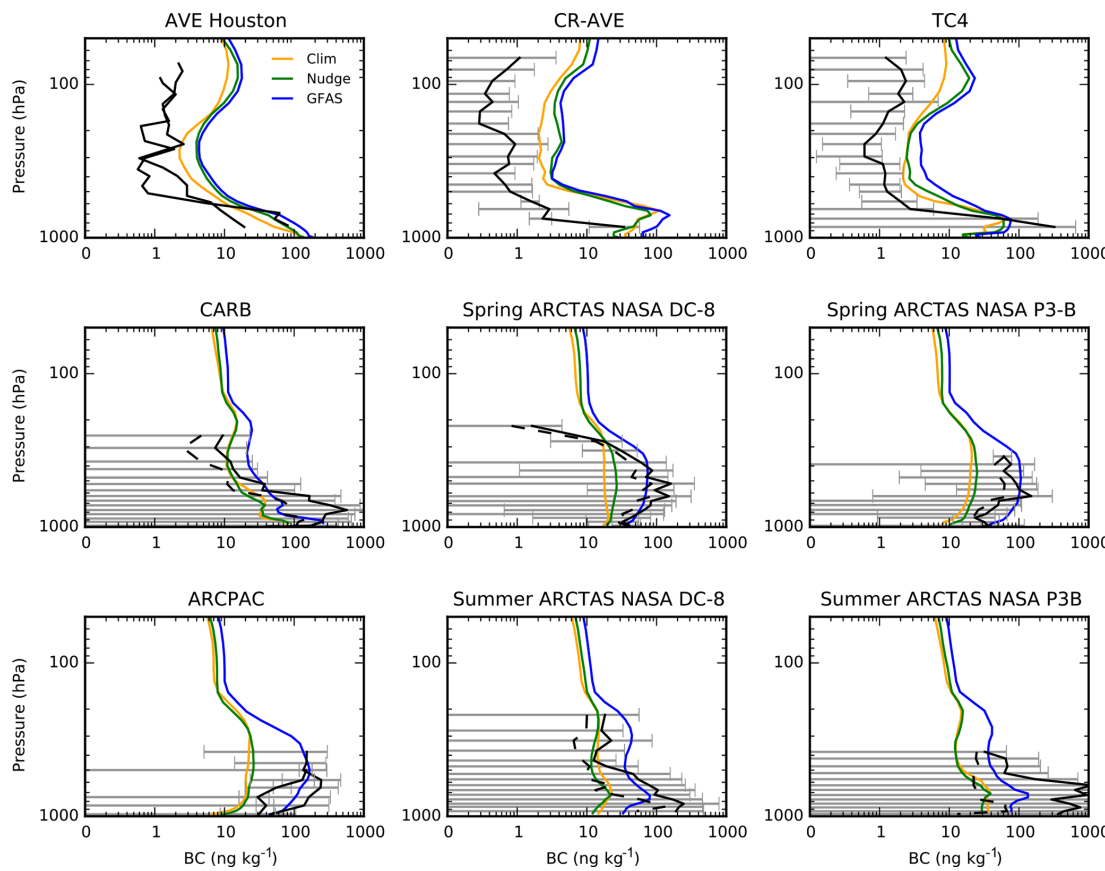


Figure 14. Vertical profiles of observed concentrations of BC (black) and collocated simulated concentrations from the three simulations: CLIM (orange), NUDGE (green), and GFAS (blue). The observations are provided for nine locations and seasons (see Fig. 2) (Koch et al., 2009). Observations are averaged for the respective campaigns (standard deviations are provided where available) and mean (solid black) and median (dashed black) profiles are shown for some campaigns. Model outputs (monthly averages) are sampled over specific points in each region.

simulated BC aerosol also has a similar negative bias it is more likely that some combustion sources that contribute to both the BC and OC concentrations are underestimated by the model. The negative bias is reduced in the GFAS simulation in which both BC and OC emissions are enhanced. The correlation (R) between OC model results and observations (between 0.49 and 0.57) is lower than for sulfate, for which $R = 0.92$ for IMPROVE stations alone (not shown).

For the aircraft measurements the comparison with modeled OC (Fig. 16) provides a similar picture. While the modeled OC values are still within the measurement variability indicated in the figure, for the ACE-Asia, ARCTAS (Arctic region), DODO and DABEX (both West Africa), and VOCALS (Pacific) campaigns the GFAS results clearly show higher OC concentrations compared to the NUDGE and CLIM experiments. The higher concentrations agree better with the measurements for the Arctic, but for the African and Pacific concentrations the GFAS results overestimate the measured values. For the AMMA campaign the modeled sulfate concentrations considerably overestimate the measure-

ments for the NUDGE and CLIM simulations, but here a good agreement is found for GFAS. For aircraft measurements in North America and Europe the model partly underestimates OC concentrations near the surface considerably, but the agreement at higher altitudes is well within the uncertainty range of the observations.

5.6 Mineral dust

Model results for mineral dust are compared to AOT and AE retrievals at selected AERONET stations that are dominated by dust aerosol and dust concentrations measured at surface stations from the AEROCE and SEAREX programs. The locations of the in situ measurements are illustrated in Fig. 17.

Modeled AOT and AE for the CLIM and NUDGE experiments are compared for AERONET stations that were labeled as “dusty” by Huneeus et al. (2011). AOT time series for a subset of these stations are shown in Fig. 18. Overall the AOTs are higher for stations influenced by dust compared to the non-dust stations in Fig. 4, exceeding monthly mean values of 1 in multiple instances. The temporal changes

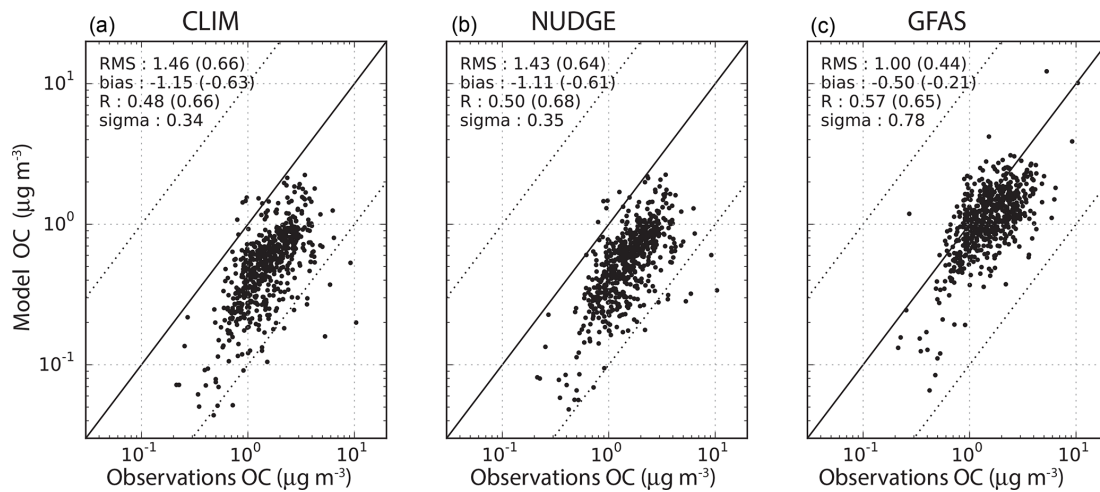


Figure 15. Scatterplot of observed surface concentrations of OC from the IMPROVE network and collocated simulated daily concentrations from the CLIM (a), NUDGE (b), and GFAS (c) simulations. The yearly mean is calculated from January 2003 to December 2004 for all available stations (see Fig. 2 for the location of the stations). The statistical parameters are calculated as in Fig. 5.

from daily to interannual timescales in dust AOT are strongly controlled by the surface wind speeds in dust source regions that lead to dust emissions if a wind speed threshold is exceeded. Therefore, the monthly and interannual changes in AOT in dust-controlled regions are clearly better matched to the AERONET observations for NUDGE compared to the CLIM simulation. This is also evident in Fig. 19 that relates monthly AOTs averaged for days when measurements were available at the respective AERONET stations. The correlation coefficient between annual AOTs for model results and observations is 0.39 and 0.56 for the CLIM and NUDGE simulations, respectively. This is expected as the nudged meteorology should capture individual dust events better than the meteorology from the free model run. The model results have a slight negative bias, indicating insufficient dust amounts. The negative bias is partly due to discrepancies at Arabian stations, where dust sources may not be sufficiently characterized. RMS (0.27 and 0.28) and negative bias (-0.13 and -0.16) are similar for both experiments. The simulated AE at the AERONET stations (Fig. 20) shows a better correlation (0.62 for CLIM and 0.72 for NUDGE) but also a considerable positive bias (0.26 and 0.27) for all regions, again indicating too-small particle sizes or underestimated coarse-mode dust particles in the model. In Fig. 20 it is evident that the AE at Caribbean stations impacted by long-range transport (blue symbols) has a lower negative bias, indicating a better agreement in particle sizes compared to near-source regions, which points to too-low coarse-mode aerosol that would have been removed by gravitational settling in the remote regions.

Huneeus et al. (2011) performed a similar evaluation for monthly averages of dust simulations by several AeroCom models. Compared to that study, the correlations of the average AOT and AE results and observations from

the NUDGE simulation are higher compared to the earlier version ECHAM5–HAM2, but slightly lower than for the AeroCom median. Pearson correlation coefficients for the NUDGE simulations were 0.56, while Huneeus et al. (2011) found correlation coefficients of $R = 0.23$ for monthly averaged AOTs for the previous version ECHAM5–HAM but as much as 0.85 for the AeroCom median. The spatial correlations of ECHAM5–HAM AE were 0.74 and 0.81 for the AeroCom median. This is in the range of the results for the NUDGE experiment for which the correlation coefficient for monthly averaged AE is 0.72, as stated above. Thus, while the agreement with AERONET AOTs in dusty regions improved compared to the previous model version, the agreement in AEs remained about the same.

Other than for the AOT at AERONET sites with strong dust influence, the comparison of model results and measurements of monthly mean dust surface concentrations at the AEROCE and SEAREX sites (Fig. 21) shows some instances in which the disagreement at some stations exceeds an order of magnitude. It should be kept in mind that for the surface concentration results – in contrast to the AERONET comparisons – the time periods of simulations and observations were different.

As for AOT, the correlation coefficient R for the NUDGE simulation is 0.64, which is again clearly better than for CLIM results with $R = 0.49$. The sigma values reflecting the ratios of simulated and observed variabilities at the station locations are 1.2 and 2.5 for NUDGE and CLIM, respectively. The variabilities in the model surface concentrations are higher than the observations, which is contrast to the AERONET comparisons. The annually averaged concentrations can be compared to the values for the same comparison by Huneeus et al. (2011) (Table 4). Their correlations of annual averaged concentrations of 0.84 for CLIM and

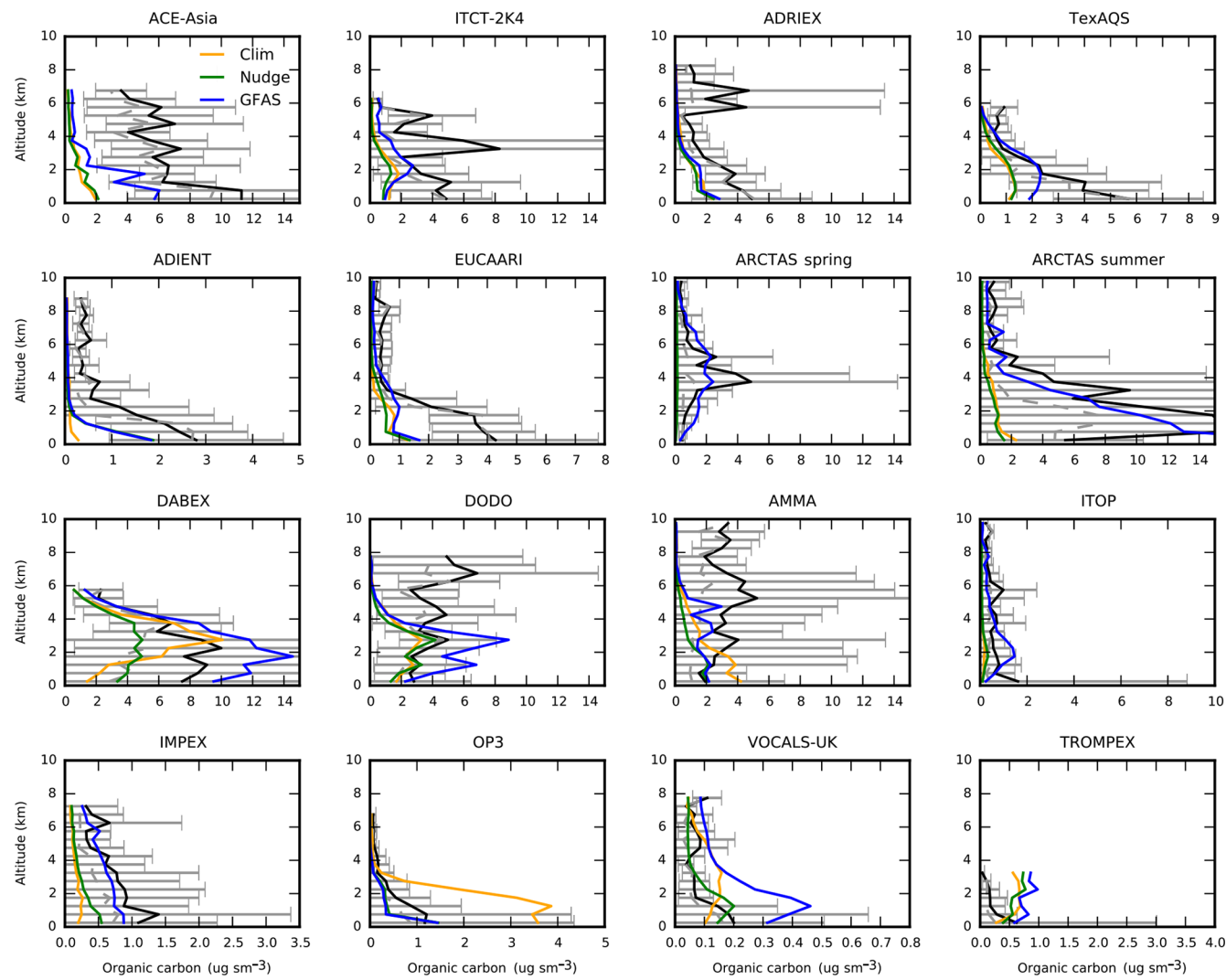


Figure 16. As Fig. 12 for OC aerosol.

0.91 for NUDGE are higher than the previous model version ECHAM5–HAM ($R = 0.8$) and for the NUDGE simulation also better than the AeroCom median with $R = 0.82$. NUDGE results also have a lower bias, but RMS is higher for CLIM and similar for NUDGE compared to the results from ECHAM5–HAM.

5.7 Sea salt aerosol

In ECHAM6.3–HAM2.3 several sea salt emission schemes can be selected. A new emission scheme is used for the simulations in this work. It is based on Long et al. (2011) and includes a temperature dependence according to Sofiev et al. (2011) that was derived as a parameterization from laboratory measurements. The temperature dependence may be a consequence of the temperature dependence of the seawater surface tension, or it may be due to the higher solubility of air entrained in the surface water at colder temperatures lead-

ing to less bubble production and thus lower sea salt aerosol emissions. The temperature correction causes an increase in sea salt aerosol mass emission fluxes in regions where sea surface temperatures are above 20°C and a decrease at lower temperatures. At the same time, emission fluxes increase at lower and decrease at higher sea surface temperatures compared to the temperature-independent parameterization.

The results for surface concentration and size distribution are compared for four sea salt emission schemes that can be selected in the HAMMOZ namelist. Compared are results from nudged simulations using the previous ECHAM–HAM default scheme by Guelle et al. (2001) (Guelle), the often used emission scheme by Gong (2003) (Gong), and a model version in which the Gong scheme is modified by the temperature dependence according to Sofiev et al. (2011) (Gong-T). The differences in the emission characteristics of the different emission schemes and their performances in a regional aerosol transport model are shown in Barthel et al.

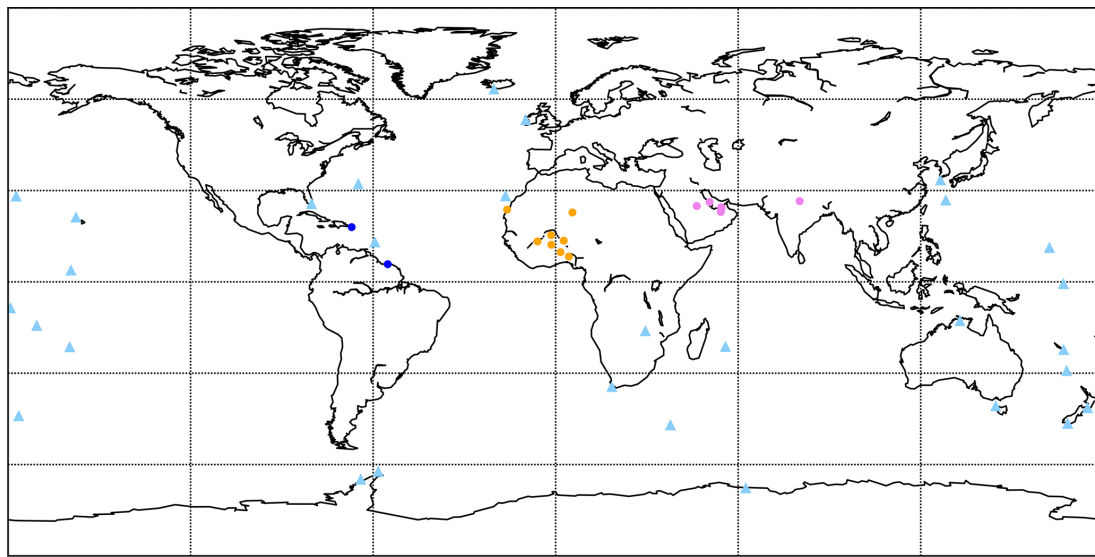


Figure 17. Locations of stations used for the evaluation of dust (DU) and sea salt (SS) aerosol. Triangles: AEROCE and SEAREX stations with dust and sea salt surface measurements. Circles: AERONET stations labeled as “dusty” by Huneeus et al. (2011). Yellow: North Africa; pink: Middle East and Asia; dark blue: Central America; light blue: marine stations.

Table 4. Comparison between observed and simulated ECHAM6–HAM2 annual average dust surface concentrations at the locations of the AEROCE and SEAREX stations (see Fig. 17).

Data	CLIM	NUDGE	ECHAM5–HAM*	AeroCom median*
Surface dust concentration				
Correlation coefficient	0.84	0.91	0.80	0.82
Absolute mean bias	2.87	-0.29	-2.18	-1.45
Relative mean bias	0.26	0.14	-0.46	-0.39
RMS	17.3	3.8	4.1	3.1
Sigma (mod. SD / obs. SD)	2.9	1.1	0.4	0.7

* Cited from Huneeus et al. (2011).

(2019). Higher emission fluxes for particle sizes above $2\text{ }\mu\text{m}$ are expected for Guelle and Gong compared to the NUDGE parameterization because, in contrast to those parameterizations, spume drops contributing to large particle sizes are not included in the Long et al. (2011) emission scheme. Spume drops are torn off wave crests at high wind speeds, and thus their emission is related to wave breaking. These spume droplets have particle sizes of the order of $20\text{ }\mu\text{m}$ or larger (see, e.g., Andreas et al., 2010). Due to their large sizes they sediment quickly and their atmospheric lifetimes are very short, so spume droplets are not expected to be relevant for the atmospheric aerosol burden. Also, their impact on both radiative fluxes and as CCN is expected to be small. Nevertheless, including spume drop formation in the sea salt emission parameterization may lead to high emission mass fluxes, while sea salt aerosol number concentrations are not strongly affected by the spume drop formation. The omission of spume drops in the new sea salt emission parameteriza-

tion may explain much lower sea salt emission fluxes in this model version compared to earlier versions.

Sea salt aerosol has only a minor influence on AOTs except over the Southern Ocean where the contribution of anthropogenic and dust aerosols is small. Simulations with the different sea salt emission schemes in ECHAM6.3–HAM2.3 are compared with measurements from the AERONET Maritime Network (MAN) (http://aeronet.gsfc.nasa.gov/new_web/maritime_aerosol_network.html, last access: 1 March 2019, Smirnov et al., 2009) taken on individual research cruises. Compared are the simulated and measured AOTs for NUDGE and Guelle for the year 2007 that had good data coverage (Fig. 22a and b). While both simulations have a slight negative bias, the rank correlation for NUDGE is 0.83, which is better than the Guelle AOT results with $R = 0.79$. In addition, for AERONET stations in the Southern Ocean the daily AOTs and AEs are shown in Fig. 22c and d for collocated model results. While it is evident that the AOT is better matched for CLIM, NUDGE, and

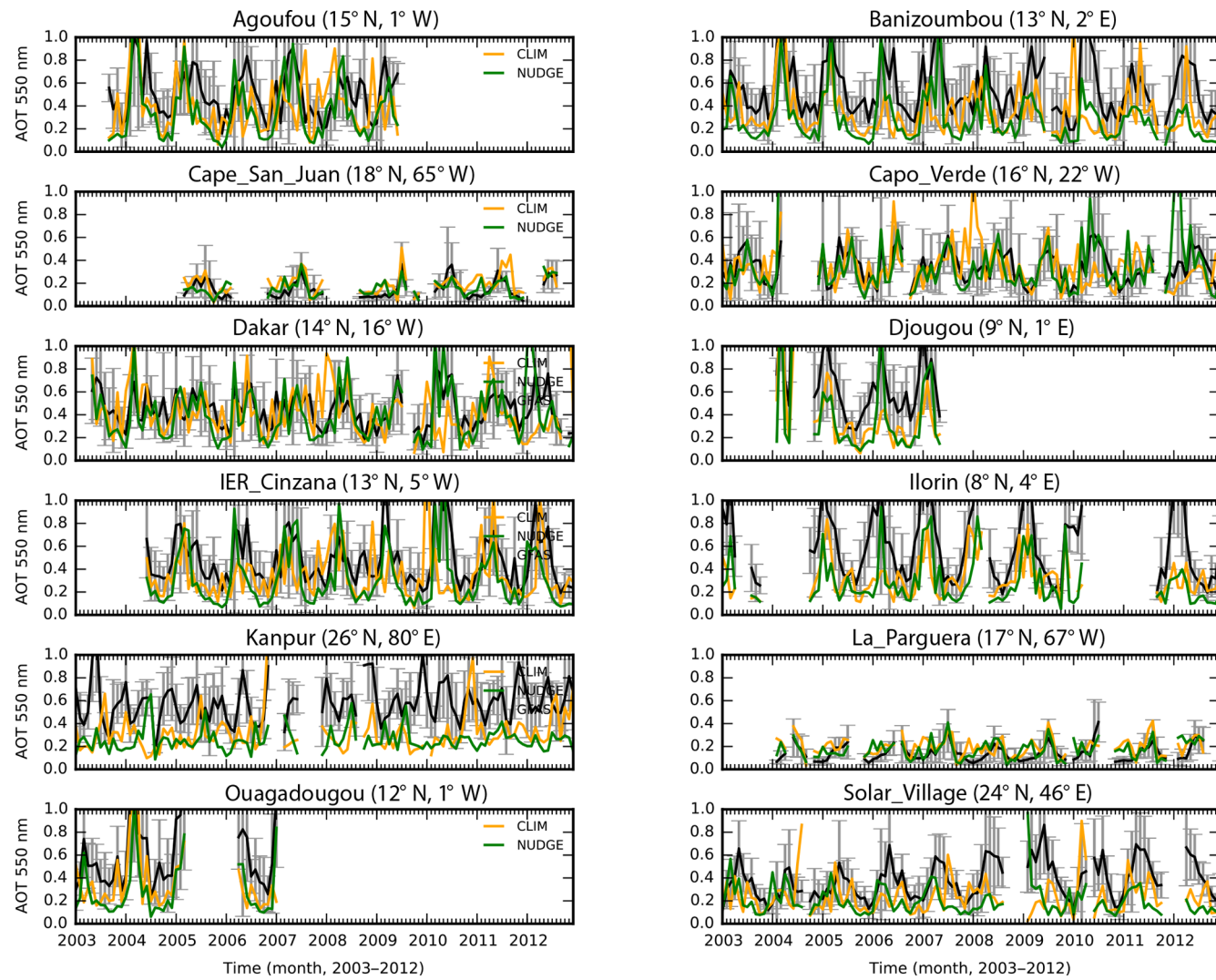


Figure 18. Time series of AOT at selected stations labeled as “dusty” by Huneeus et al. (2011) for the years 2003 to 2012 for the CLIM and NUDGE simulations.

GFAS results compared to the Guelle results that overestimate AOTs, the results obtained using the new model sea salt emissions overestimate AE. This again points toward missing coarse-mode aerosols in the model due to the neglect of sea salt aerosol formed by spume droplets.

The model results were also evaluated against sea salt surface concentrations measured at AEROCE and SEAREX stations using simulation results for the year 2010 (Fig. 17). Only stations where the sea salt concentrations remain below $100 \mu\text{m}^{-3}$ are considered, as higher concentrations indicate local influences that cannot be captured by the model. The scatterplots show that the temperature dependence improved the correlation between monthly measurements and model simulations (Fig. 23). Correlations are still worse than those for the dust surface concentrations, as the station measurements may be influenced by local conditions not well captured by the model, but increased from $R = 0.18\text{--}0.19$ for

Guelle and Gong to $R = 0.31$ for NUDGE and Gong-T. The bias is negative for temperature-dependent emissions. RMS errors are similar for the different simulation results. For the time series of a subset of individual stations it can be seen that the model results mostly stay within the error bars indicating the standard deviation of the observations (Fig. 24). Most differences are evident for the treatment of temperature in the different simulations. For stations between 45°N and 45°S the different model setups provide similar results, and no individual emission scheme performs best for all stations. For high-latitude stations north of 45°N or south of 45°S the surface concentrations computed in the simulations that include a temperature dependence (NUDGE, Gong-T) clearly match the observed sea salt concentrations better than the results using the original Gong and Guelle emission schemes without temperature correction.

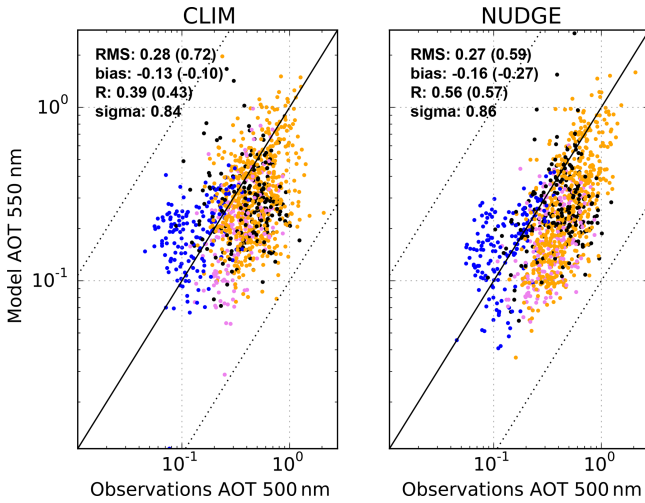


Figure 19. Scatterplot of observed versus simulated monthly mean AOT in dusty regions based on daily results at the AERONET stations shown in Fig. 17. The simulated monthly means are constructed by sampling the collocated model from daily outputs for the same days as the observations. Stations are color coded depending on the regions to which they belong as shown in Fig. 17. Yellow: North Africa; pink: Middle East and Asia; dark blue: Central America; light blue: marine stations. For each comparison the root mean square error (RMS; normalized RMS in parentheses), the Pearson correlation coefficient (R , on log scale in parentheses), the absolute bias (normalized bias), and the ratio between simulated and observed standard deviation (sigma) are given.

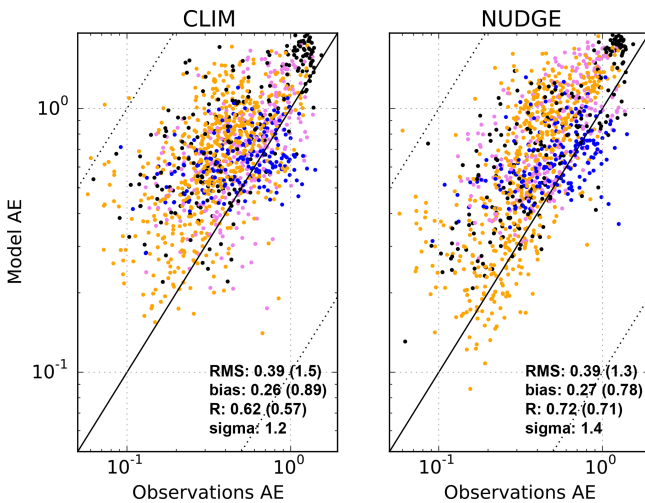


Figure 20. As Fig. 19 for the Ångstrom exponent.

Not only concentrations but also particle size dependences are influenced by the different sea salt emission parameterizations. As with AOTs, the oceanic aerosol size distribution is strongly influenced by aerosols other than sea salt aerosol, e.g., anthropogenic or natural sulfates. For comparison with the compilation of aerosol particle size distributions at different marine sites compiled by Heintzenberg et al. (2000), only

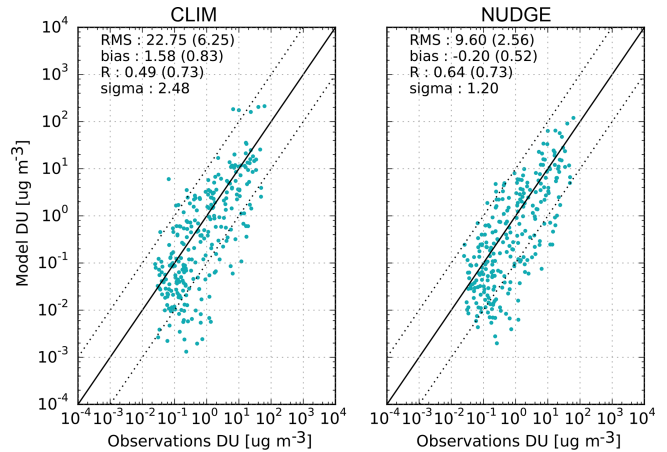


Figure 21. Scatterplot of observed versus simulated monthly mean dust surface concentrations at the AEROCE and SEAREX stations shown in Fig. 17. Simulated monthly means were constructed from the daily mean outputs sampled on the same days of the observations and collocated to the observation position for the time period 2003–2012.

for the region 40–60° S are discernible differences for the different model results found (Fig. 25). Only in this region does the sea salt distribution have a notable impact compared to anthropogenic and biomass burning smoke contributions to aerosol number size distributions in other oceanic regions. The temperature-dependent results are shifted to smaller particle sizes compared to the results from modeled sea salt emissions that do not include a temperature dependence. In contrast to mass emissions, the number size concentration for accumulation-mode particles is higher in the NUDGE setup using the Long et al. (2011) parameterization than for the other model results and best matches the observed number concentrations. Considering the evaluation of both mass concentration and particle number concentration, the parameterization by Long et al. (2011), including a temperature dependence, can be considered an overall reasonable choice. This is also in agreement with the results by Barthel et al. (2019), who evaluated simulations of a regional aerosol transport model using the same sea salt emission parameterizations with surface measurements.

6 Conclusions and outlook

The aerosol–chemistry–climate model ECHAM–HAMMOZ has been updated and improved since the previous release version (Zhang et al., 2012). The aerosol part ECHAM6.3–HAM2.3 is evaluated against a standard set of aerosol observations including AOT and AE from sun photometer measurements, particle size distribution, and in situ measurements of mass concentrations of different aerosol species including aircraft measurements. A comparison against the previous results was not the main focus of this paper since

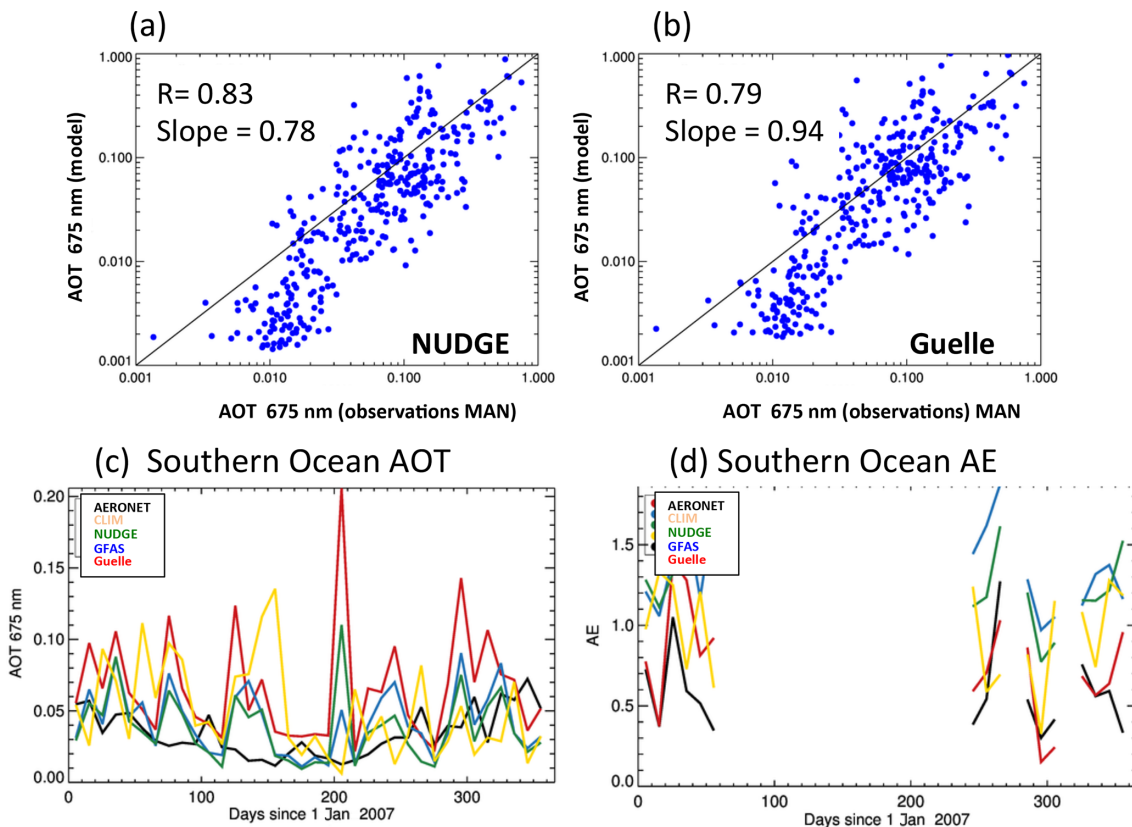


Figure 22. Comparison of model results with sun photometer data for (a) AOT at stations of the AERONET Maritime Aerosol Network for NUDGE simulations (2007); (b) as (a) for simulations with the Guelle sea salt emission parameterization; (c) time series for 2007 comparing AOT from AERONET stations for NUDGE, CLIM, GFAS, and Guelle simulations in the Southern Ocean; (d) as (c) for AE.

both the host model ECHAM and the aerosol model have been updated at the same time. The aerosol model can be used in combination with the chemistry module in the ECHAM–HAMMOZ setup (Schultz et al., 2018) or with a simplified sulfur chemistry, which is evaluated in this publication. The alternative aerosol setup with the sectional aerosol scheme ECHAM6.3–HAM2.3–SALSA was evaluated by Kokkola et al. (2018).

The updates of the aerosol model include changes in the model structure, bug fixes, updates in aerosol processes including updates for aerosol water uptake and cloud activation, and updated aerosol emissions. Anthropogenic emissions of SO_2 , OC, and BC from ACCMIP and biomass burning emissions from ACCMIP or GFAS datasets can be chosen. Emissions of mineral dust now include updated Saharan dust sources and allow for coupling with the JSBACH land surface scheme. A regional tuning parameter was introduced to account for changes in the surface parameterization of the ECHAM. A new sea salt aerosol emission scheme was implemented that includes a temperature dependence of sea salt emission fluxes. Globally, the sea salt aerosol mass emission fluxes are strongly reduced compared to the standard emission scheme used in the previous version, leading to an im-

proved agreement of sea salt particle concentrations in the surface layer compared to the previous version. A positive AOT bias in the tropical ocean regions may, however, indicate too-high sea salt emissions. This could be clarified by further evaluation with profile measurements in future studies.

The model performs well in the comparison of different aspects of aerosol distribution. Using state-of-the-art anthropogenic aerosol emissions is the basis for investigations examining the role of anthropogenic aerosol changes in the climate system. Attention must also be given to carefully characterizing natural aerosol distributions. In addition to the need for understanding the distribution of natural aerosols in order to evaluate anthropogenic aerosol distributions, anthropogenic aerosol effects such as aerosol–cloud interactions depend not only on the anthropogenic enhancement of aerosols, but also on background aerosol from natural sources. Natural aerosol emissions of dust, but also sea salt or vegetation emissions, may change in a changing climate due to changing wind patterns or surface conditions. A realistic representation of the processes controlling emissions and the atmospheric distribution of natural aerosols is needed as a

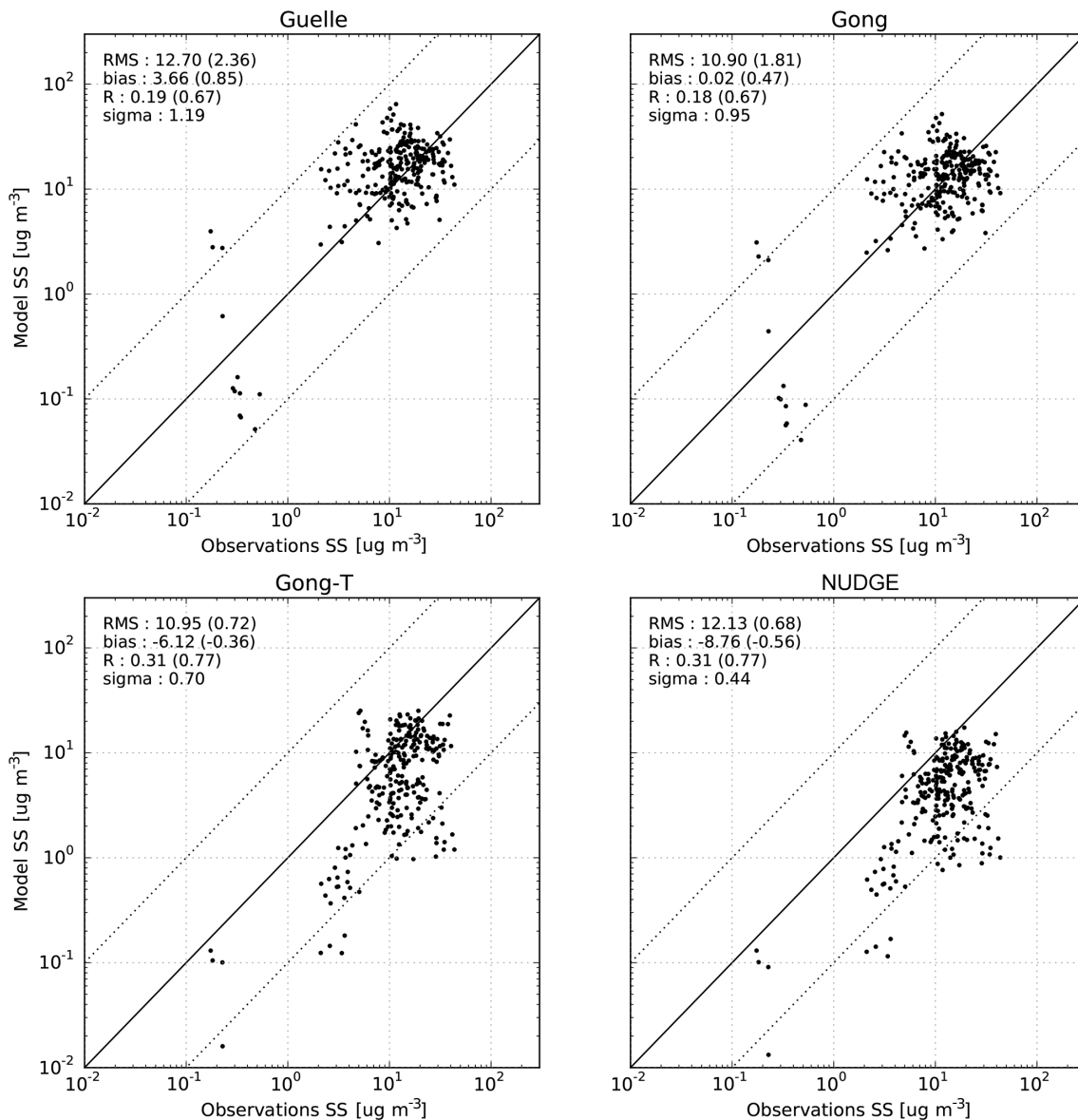


Figure 23. Scatterplot of observed versus simulated monthly mean sea salt surface concentrations at the AEROCE and SEAREX stations shown in Fig. 17 for 2010. Compared are simulations using different sea salt emission parameterizations (Guelle, Gong, Gong-T, NUDGE).

basis for reliable prognoses of aerosol–climate interactions in a changing climate.

As natural aerosol distributions are strongly impacted by dust and sea salt particle emissions, particular attention was given to updating and testing these aerosol species. In the new version of ECHAM6–HAM2 they compare more favorably to observations than in the previous version. However, due to the description of the aerosol size distribution by modes, large particle sizes may be underestimated, which is evident in the overestimate of AE in regions dominated by dust and sea salt aerosol. While neglecting part of the coarse-mode particle load may have only a minor influence on the particle number and thus CCN concentrations, mass fluxes

may be underestimated. A positive bias in the comparison of AE may also point towards an underestimate in coarse-mode aerosols emitted by biomass burning. Overall the model reproduces AOTs and sulfate concentrations at US and European sites well, but to some extent underestimates BC and OC concentrations, which may be caused by missing fossil fuel or underestimated biomass burning sources.

As expected, the model versions using nudged wind fields (NUDGE) to simulate atmospheric aerosol transport (and emissions in the case of mineral dust and sea salt) perform better in terms of reproducing the temporal variability in aerosol distributions at different timescales compared to the

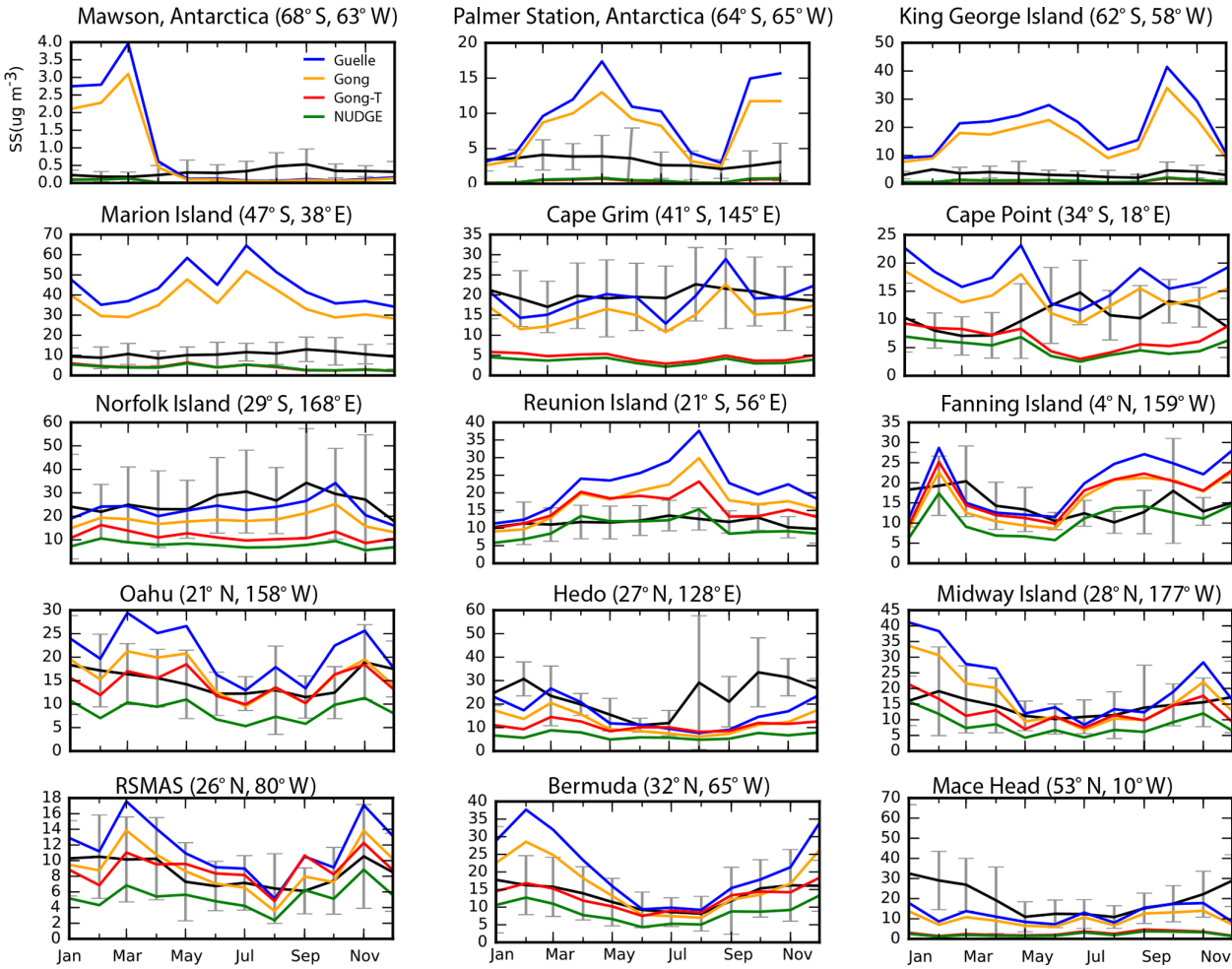


Figure 24. Time series of observed versus simulated monthly mean sea salt aerosol surface concentrations for the year 2010 spatially collocated at the AEROCE stations shown in Fig. 17. Only stations where the sea salt concentrations remain below $100 \mu\text{m}^{-3}$ are considered to exclude stations with clearly local impact.

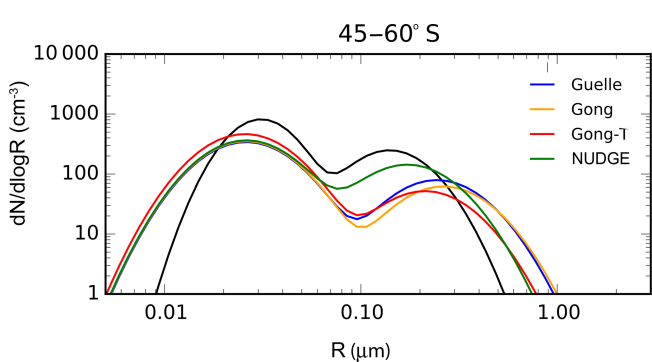


Figure 25. Size distribution of simulated and measured aerosol number concentrations in the marine boundary layer for the region $40\text{--}60^\circ \text{S}$ (as in Fig. 10) for the year 2010.

free (CLIM) runs. However, differences in the bias and variabilities in the CLIM and NUDGE simulations are small.

Even where the evaluation of aerosol distributions simulated with the updated ECHAM6.3–HAM2.3 model shows only small improvements compared to earlier model versions and discrepancies remain, such as in the underestimation of BC and OC concentrations, the use of more realistic aerosol processes and updated emissions is a prerequisite for reliable model studies of the effects and interactions of aerosols in the climate system.

Further evaluation with monitoring and field data will be performed in ongoing projects. Upcoming developments in the model will include updates in the secondary aerosol scheme and adding nitrate aerosol to the microphysics scheme.

Code availability. The ECHAM6–HAMMOZ code is maintained and made available to the scientific community under

<https://redmine.hammoz.ethz.ch/> (HAMMOZ consortium, 2017). The availability is regulated under the HAMMOZ Software Licence Agreement that can be downloaded from https://redmine.hammoz.ethz.ch/attachments/download/291/License_ECHAM-HAMMOZ_June2012.pdf (last access: 1 March 2019).

Data availability. AERONET data can be obtained with the Aerosol Robotic Network download tool at https://aeronet.gsfc.nasa.gov/cgi-bin/webtool_opera_v2_new (NASA, 2019). MODIS products are available for download from Level 1 and the Atmosphere Archive and Distribution System (LAADS) at <https://ladsweb.modaps.eosdis.nasa.gov/search/> (NASA, 2017). EMEP data are available for download at <http://ebas.nilu.no/> (Norwegian Institute for Air Research, 2015). IMPROVE data are available for download from the Federal Land Manager Environmental Database at <http://views.cira.colostate.edu/fed/DataWizard/Default.aspx> (Colorado State University, 2019). AEROCE and SEAREX data can be downloaded from https://aerocom.met.no/DATA/download/DUST_BENCHMARK_HUNEEUS2011/ (Huneeus et al., 2011). The BC aircraft measurement data are available at https://aerocom.met.no/DATA/download/BC_BENCHMARK_KOCH2009/ (Koch et al., 2009). EUSAAR size distributions can be downloaded from <https://doi.org/10.1594/PANGAEA.861856> (Asmi et al., 2011b). The aircraft data for sulfate and OC were received from several measurement teams who hold the ownership for the data.

Competing interests. The authors declare that they have no conflict of interest.

Author contributions. IT prepared the paper; DN, SF, and CSLD were instrumental in the development and testing of the model code, designed the majority of the figures, and commented on the paper; IB designed the comparison in part of the model evaluation strategy and outlined an earlier draft version of the paper; NS performed the model evaluation with MODIS data and created several figures; PS, DW, HS, SR, HK, MS, SS, SB, and BH contributed to the model development and commented on the paper; TS performed the regional tuning and testing of the dust emissions in the model and commented on the paper; ND prepared observation datasets; and UL coordinated the model development and commented on the paper.

Acknowledgements. The ECHAM–HAMMOZ model is developed by a consortium composed of ETH Zurich, the Max Planck Institute for Meteorology, Forschungszentrum Juelich, the University of Oxford, the Finnish Meteorological Institute, and the Leibniz Institute for Tropospheric Research; it is managed by the Center for Climate Systems Modeling (C2SM) at ETH Zurich. The research leading to these results has received partial funding from the Center for Climate System Modelling (C2SM) at ETH Zurich and the European Union's Seventh Framework Programme (FP7/2007–2013) project BACCHUS under grant agreement no. 603445. This work was supported by a grant from the Swiss National Supercomputing

Centre (CSCS) under project ID s652. We are grateful for computing time from the Swiss Computing Centre (CSCS), ETH Zurich, and the Deutsches Klimarechenzentrum (DKRZ). Computing resources at DKRZ were granted under project number bb1004. Philip Stier acknowledges funding from the European Union's Seventh Framework Programme (FP7/2007–2013) project BACCHUS under grant agreement 603445 and the European Research Council project ACCLAIM under grant agreement FP7280025, as well as the European Research Council project RECAP under the European Union's Horizon 2020 research and innovation program with grant agreement 724602. Harri Kokkola acknowledges support by the Academy of Finland project nos. 308292 and 307331 and Nordforsk project no. 57001. The data used are listed in the references and are available under <https://redmine.hammoz.ethz.ch> (last access: 1 March 2019). We thank the AERONET principal investigators and their staff for establishing and maintaining the sites used in this paper. IMPROVE is a collaborative association of state, tribal, and federal agencies, as well as international partners. We thank Maria Kanakidou (ECPL, University of Crete) for the help in compiling the EMEP and IMPROVE datasets. For the aircraft data we thank Colette Heald (MIT, Dept. Civil and Environmental Engineering), Hugh Coe (University of Manchester), Lynn Russell (Scripps Institution of Oceanography), Rodney Weber (Georgia Institute of Technology), Jose Jimenez (University of Colorado at Boulder), Roya Bahreini (University of Colorado – CIRES, NOAA ESRL Chemical Sciences Division), and Ann Middlebrook (NOAA ESRL Chemical Sciences Division). We are grateful for the James S. McDonnell Foundation Award for 21st Century Science, NOAA grant NA17RJ1231, National Science Foundation grants ATM-0002035, ATM-0002698, and ATM04-01611, and the NERC Global Aerosol Synthesis and Science Project (GASSP) NE/J023515/1. The US Environmental Protection Agency is the primary funding source, with contracting and research support from the National Park Service. The Air Quality Group at the University of California, Davis, is the central analytical laboratory, with 20 ion analyses provided by the Research Triangle Institute and carbon analysis provided by the Desert Research Institute. The authors thank Ron Miller and two anonymous reviewers for their constructive comments and suggestions.

The publication of this article was funded by the Open Access Fund of the Leibniz Association.

Edited by: Samuel Remy

Reviewed by: Ron L. Miller and two anonymous referees

References

- Abdul-Razzak, H. and Ghan, S.: A parameterization of aerosol activation: 2. Multiple aerosol types, *J. Geophys. Res.-Atmos.*, 105, 6837–6844, <https://doi.org/10.1029/1999JD901161>, 2000.
- Andreas, E. L., Jones, K. F., and Fairall, C. W.: Production velocity of sea spray droplets, *J. Geophys. Res.-Oceans*, 115, C12065, <https://doi.org/10.1029/2010JC006458>, 2010.
- Arimoto, R., Duce, R. A., Ray, B. J., Ellis, W. G., Cullen, J. D., and Merrill, J. T.: Trace elements in the atmosphere over the North Atlantic, *J. Geophys. Res.-Atmos.*, 100, 1199–1213, <https://doi.org/10.1029/94JD02618>, 1995.

- Asmi, A., Wiedensohler, A., Laj, P., Fjaeraa, A.-M., Sellegri, K., Birmili, W., Weingartner, E., Baltensperger, U., Zdimal, V., Zikova, N., Putaud, J.-P., Marinoni, A., Tunved, P., Hansson, H.-C., Fiebig, M., Kivekäs, N., Lihavainen, H., Asmi, E., Ulevicius, V., Aalto, P. P., Swietlicki, E., Kristensson, A., Mihalopoulos, N., Kalivitis, N., Kalapov, I., Kiss, G., de Leeuw, G., Henzing, B., Harrison, R. M., Beddows, D., O'Dowd, C., Jennings, S. G., Flentje, H., Weinhold, K., Meinhardt, F., Ries, L., and Kulmala, M.: Number size distributions and seasonality of submicron particles in Europe 2008–2009, *Atmos. Chem. Phys.*, 11, 5505–5538, <https://doi.org/10.5194/acp-11-5505-2011>, 2011a.
- Asmi, A., Wiedensohler, A., Laj, P., Fjaeraa, A.-M., Sellegri, K., Birmili, W., Weingartner, E., Baltensperger, U., Zdimal, V., Zikova, N., Putaud, J.-P., Marinoni, A., Tunved, P., Hansson, H.-C., Fiebig, M., Kivekäs, N., Lihavainen, H., Asmi, E., Ulevicius, V., Aalto, P., Swietlicki, E., Kristensson, A., Mihalopoulos, N., Kalivitis, N., Kalapov, I., Kiss, G., de Leeuw, G., Henzing, B., Harrison, R. M., Beddows, D., O'Dowd, C., Jennings, S. G., Flentje, H., Weinhold, K., Meinhardt, F., Ries, L., and Kulmala, M.: EUSAAR size distribution analysis database. PANGAEA, <https://doi.org/10.1594/PANGAEA.861856>, 2011b.
- Barthel, S., Tegen, I., and Wolke, R.: Do new sea spray aerosol source functions improve the results of a regional aerosol model?, *Atmos. Environ.*, 198, 265–278, <https://doi.org/10.1016/j.atmosenv.2018.10.016>, 2019.
- Bauer, S. E., Tsigaridis, K., and Miller, R.: Significant atmospheric aerosol pollution caused by world food cultivation, *Geophys. Res. Lett.*, 43, 5394–5400, <https://doi.org/10.1002/2016GL068354>, 2016.
- Berrisford, P., Kallberg, P., Kobayashi, S., Dee, D., Uppala, S., Simmons, A. J., Poli, P., and Sato, H.: Atmospheric conservation properties in ERA Interim, *Q. J. Roy. Meteor. Soc.*, 137, 1381–1399, <https://doi.org/10.1002/qj.864>, 2011.
- Bond, T. and Bergstrom, R.: Light Absorption by Carbonaceous Particles: An Investigative Review, *Aerosol Sci. Tech.*, 40, 27–67, <https://doi.org/10.1080/02786820500421521>, 2006.
- Boucher, O., Randall, D., Artaxo, P., Bretherton, C., Feingold, G., Forster, P., Kerminen, V.-M., Kondo, Y., Liao, H., Lohmann, U., Rasch, P., Satheesh, S. K., Sherwood, S., Stevens, B., and Zhang, X. Y.: Clouds and aerosols, Cambridge University Press, Cambridge, UK, 571–657, <https://doi.org/10.1017/CBO9781107415324.016>, 2013.
- Cheng, T., Peng, Y., Feichter, J., and Tegen, I.: An improvement on the dust emission scheme in the global aerosol-climate model ECHAM5-HAM, *Atmos. Chem. Phys.*, 8, 1105–1117, <https://doi.org/10.5194/acp-8-1105-2008>, 2008.
- Colorado State University: IMPROVE data, Federal Land Manager Environmental Database, available at: <http://views.cira.colostate.edu/fed/DataWizard/Default.aspx>, last access: 1 March 2019.
- Croft, B., Lohmann, U., Martin, R. V., Stier, P., Wurzler, S., Feichter, J., Posselt, R., and Ferrachat, S.: Aerosol size-dependent below-cloud scavenging by rain and snow in the ECHAM5-HAM, *Atmos. Chem. Phys.*, 9, 4653–4675, <https://doi.org/10.5194/acp-9-4653-2009>, 2009.
- Croft, B., Lohmann, U., Martin, R. V., Stier, P., Wurzler, S., Feichter, J., Hoose, C., Heikkilä, U., van Donkelaar, A., and Ferrachat, S.: Influences of in-cloud aerosol scavenging parameterizations on aerosol concentrations and wet deposition in ECHAM5-HAM, *Atmos. Chem. Phys.*, 10, 1511–1543, <https://doi.org/10.5194/acp-10-1511-2010>, 2010.
- Croft, B., Martin, R. V., Leaitch, W. R., Tunved, P., Breider, T. J., D'Andrea, S. D., and Pierce, J. R.: Processes controlling the annual cycle of Arctic aerosol number and size distributions, *Atmos. Chem. Phys.*, 16, 3665–3682, <https://doi.org/10.5194/acp-16-3665-2016>, 2016.
- Dentener, F., Kinne, S., Bond, T., Boucher, O., Cofala, J., Generoso, S., Ginoux, P., Gong, S., Hoelzemann, J. J., Ito, A., Marelli, L., Penner, J. E., Putaud, J.-P., Textor, C., Schulz, M., van der Werf, G. R., and Wilson, J.: Emissions of primary aerosol and precursor gases in the years 2000 and 1750 prescribed data-sets for AeroCom, *Atmos. Chem. Phys.*, 6, 4321–4344, <https://doi.org/10.5194/acp-6-4321-2006>, 2006.
- Dubovik, O. and King, M. D.: A flexible inversion algorithm for retrieval of aerosol optical properties from Sun and sky radiance measurements, *J. Geophys. Res.-Atmos.*, 105, 20673–20696, <https://doi.org/10.1029/2000JD900282>, 2000.
- Feichter, J., Kjellstrom, E., Rodhe, H., Dentener, F., Lelieveld, J., and Roelofs, G.-J.: Simulation of the tropospheric sulfur cycle in a global climate model, *Atmos. Environ.*, 30, 1693–1707, 1996.
- Folini, D. and Wild, M.: Aerosol emissions and dimming/brightening in Europe: Sensitivity studies with ECHAM5-HAM, *J. Geophys. Res.-Atmos.*, 116, d21104, <https://doi.org/10.1029/2011JD016227>, 2011.
- Gasparini, B. and Lohmann, U.: Why cirrus cloud seeding cannot substantially cool the planet, *J. Geophys. Res.-Atmos.*, 121, 4877–4893, <https://doi.org/10.1002/2015JD024666>, 2016.
- Gong, S. L.: A parameterization of sea salt aerosol source function for sub- and super-micron particles, *Global Biogeochem. Cy.*, 17, 1097, <https://doi.org/10.1029/2003GB002079>, 2003.
- Guelle, W., Schulz, M., Balkanski, Y., and Dentener, F.: Influence of the source formulation on modeling the atmospheric global distribution of sea salt aerosol, *J. Geophys. Res.-Atmos.*, 106, 27509–27524, <https://doi.org/10.1029/2001JD900249>, 2001.
- Guenther, A. B., Jiang, X., Heald, C. L., Sakulyanontvittaya, T., Duhl, T., Emmons, L. K., and Wang, X.: The Model of Emissions of Gases and Aerosols from Nature version 2.1 (MEGAN2.1): an extended and updated framework for modeling biogenic emissions, *Geosci. Model Dev.*, 5, 1471–1492, <https://doi.org/10.5194/gmd-5-1471-2012>, 2012.
- HAMMOZ consortium: ECHAM-HAMMOZ model data, available at: https://redmine.hammoz.ethz.ch/projects/hammoz/repository/show/echam6-hammoz/branches/fmi/fmi_trunk, last access: 20 June 2017.
- Heald, C. L., Coe, H., Jimenez, J. L., Weber, R. J., Bahreini, R., Middlebrook, A. M., Russell, L. M., Jolley, M., Fu, T.-M., Allan, J. D., Bower, K. N., Capes, G., Crosier, J., Morgan, W. T., Robinson, N. H., Williams, P. I., Cubison, M. J., DeCarlo, P. F., and Dunlea, E. J.: Exploring the vertical profile of atmospheric organic aerosol: comparing 17 aircraft field campaigns with a global model, *Atmos. Chem. Phys.*, 11, 12673–12696, <https://doi.org/10.5194/acp-11-12673-2011>, 2011.
- Heinold, B., Tegen, I., Schepanski, K., and Banks, J. R.: New developments in the representation of Saharan dust sources in the aerosol-climate model ECHAM6-HAM2, *Geosci. Model Dev.*, 9, 765–777, <https://doi.org/10.5194/gmd-9-765-2016>, 2016.
- Heintzenberg, J., Covert, D. C., and Van Dingenen, R.: Size distribution and chemical composition of marine aerosols:

- a compilation and review, *Tellus B*, 52, 1104–1122, <https://doi.org/10.1034/j.1600-0889.2000.00136.x>, 2000.
- Henrot, A.-J., Stanelle, T., Schröder, S., Siegenthaler, C., Taraborrelli, D., and Schultz, M. G.: Implementation of the MEGAN (v2.1) biogenic emission model in the ECHAM6-HAMMOZ chemistry climate model, *Geosci. Model Dev.*, 10, 903–926, <https://doi.org/10.5194/gmd-10-903-2017>, 2017.
- Holben, B. N., Eck, T. F., Slutsker, I., Tanre, D., Buis, J. P., Setzer, A., Vermote, E., Reagan, J. A., Kaufman, Y., Nakajima, T., Lavenue, F., Jankowiak, I., and Smirnov, A.: AERONET-A Federated Instrument Network and Data Archive for Aerosol Characterization, *Remote Sens. Environ.*, 66, 1–16, [https://doi.org/10.1016/S0034-4257\(98\)00031-5](https://doi.org/10.1016/S0034-4257(98)00031-5), 1998.
- Holben, B. N., Eck, T. E., Slutsker, I., Smirnov, A., Sinyuk, A., Schafer, J., Giles, D., and Dubovik, O.: Aeronet's Version 2.0 quality assurance criteria, *Proc. SPIE*, 6408, 64080Q, <https://doi.org/10.1117/12.706524>, 2006.
- Huneeus, N., Schulz, M., Balkanski, Y., Griesfeller, J., Prospero, J., Kinne, S., Bauer, S., Boucher, O., Chin, M., Dentener, F., Diehl, T., Easter, R., Fillmore, D., Ghan, S., Ginoux, P., Grini, A., Horowitz, L., Koch, D., Krol, M. C., Landing, W., Liu, X., Mahowald, N., Miller, R., Morcrette, J.-J., Myhre, G., Penner, J., Perlitz, J., Stier, P., Takemura, T., and Zender, C. S.: Global dust model intercomparison in AeroCom phase I, *Atmos. Chem. Phys.*, 11, 7781–7816, <https://doi.org/10.5194/acp-11-7781-2011>, 2011.
- Hyer, E. J., Reid, J. S., and Zhang, J.: An over-land aerosol optical depth data set for data assimilation by filtering, correction, and aggregation of MODIS Collection 5 optical depth retrievals, *Atmos. Meas. Tech.*, 4, 379–408, <https://doi.org/10.5194/amt-4-379-2011>, 2011.
- Iacono, M., Delamere, J., Mlawer, E., Shephard, M., Clough, S., and Collins, W.: Radiative forcing by long-lived greenhouse gases: Calculations with the AER radiative transfer models, *J. Geophys. Res.-Atmos.*, 113, D13103, <https://doi.org/10.1029/2008JD009944>, 2008.
- Inness, A., Baier, F., Benedetti, A., Bouarar, I., Chabriat, S., Clark, H., Clerbaux, C., Coheur, P., Engelen, R. J., Errera, Q., Flemming, J., George, M., Granier, C., Hadji-Lazaro, J., Huijnen, V., Hurtmans, D., Jones, L., Kaiser, J. W., Kapsomenakis, J., Lefever, K., Leitão, J., Razinger, M., Richter, A., Schultz, M. G., Simmons, A. J., Suttie, M., Stein, O., Thépaut, J.-N., Thouret, V., Vrekoussis, M., Zerefos, C., and the MACC team: The MACC reanalysis: an 8 yr data set of atmospheric composition, *Atmos. Chem. Phys.*, 13, 4073–4109, <https://doi.org/10.5194/acp-13-4073-2013>, 2013.
- Jiao, C., Flanner, M. G., Balkanski, Y., Bauer, S. E., Bellouin, N., Berntsen, T. K., Bian, H., Carslaw, K. S., Chin, M., De Luca, N., Diehl, T., Ghan, S. J., Iversen, T., Kirkevåg, A., Koch, D., Liu, X., Mann, G. W., Penner, J. E., Pitari, G., Schulz, M., Seland, Ø., Skeie, R. B., Steenrod, S. D., Stier, P., Takemura, T., Tsigaridis, K., van Noije, T., Yun, Y., and Zhang, K.: An AeroCom assessment of black carbon in Arctic snow and sea ice, *Atmos. Chem. Phys.*, 14, 2399–2417, <https://doi.org/10.5194/acp-14-2399-2014>, 2014.
- Kaiser, J. W., Heil, A., Andreae, M. O., Benedetti, A., Chubarova, N., Jones, L., Morcrette, J.-J., Razinger, M., Schultz, M. G., Suttie, M., and van der Werf, G. R.: Biomass burning emissions estimated with a global fire assimilation system based on observed fire radiative power, *Biogeosciences*, 9, 527–554, <https://doi.org/10.5194/bg-9-527-2012>, 2012.
- Kazil, J., Stier, P., Zhang, K., Quaas, J., Kinne, S., O'Donnell, D., Rast, S., Esch, M., Ferrachat, S., Lohmann, U., and Feichter, J.: Aerosol nucleation and its role for clouds and Earth's radiative forcing in the aerosol-climate model ECHAM5-HAM, *Atmos. Chem. Phys.*, 10, 10733–10752, <https://doi.org/10.5194/acp-10-10733-2010>, 2010.
- Kazil, J., Zhang, K., Stier, P., Feichter, J., Lohmann, U., and O'Brien, K.: The present-day decadal solar cycle modulation of Earth's radiative forcing via charged $\text{H}_2\text{SO}_4/\text{H}_2\text{O}$ aerosol nucleation, *Geophys. Res. Lett.*, 39, 102805, <https://doi.org/10.1029/2011GL050058>, 2012.
- King, M. D., Kaufman, Y. J., Tanré, D., and Nakajima, T.: Remote Sensing of Tropospheric Aerosols from Space: Past, Present, and Future, *B. Am. Meteorol. Soc.*, 80, 2229–2260, [https://doi.org/10.1175/1520-0477\(1999\)080<2229:RSOTAF>2.0.CO;2](https://doi.org/10.1175/1520-0477(1999)080<2229:RSOTAF>2.0.CO;2), 1999.
- Kinne, S., O'Donnell, D., Stier, P., Kloster, S., Zhang, K., Schmidt, H., Rast, S., Giorgetta, M., Eck, T., and Stevens, B.: MACv1: A new global aerosol climatology for climate studies, *J. Adv. Model. Earth Sy.*, 5, 704–740, <https://doi.org/10.1002/jame.20035>, 2013.
- Koch, D., Schulz, M., Kinne, S., McNaughton, C., Spackman, J. R., Balkanski, Y., Bauer, S., Berntsen, T., Bond, T. C., Boucher, O., Chin, M., Clarke, A., De Luca, N., Dentener, F., Diehl, T., Dubovik, O., Easter, R., Fahey, D. W., Feichter, J., Fillmore, D., Freitag, S., Ghan, S., Ginoux, P., Gong, S., Horowitz, L., Iversen, T., Kirkevåg, A., Klimont, Z., Kondo, Y., Krol, M., Liu, X., Miller, R., Montanaro, V., Moteki, N., Myhre, G., Penner, J. E., Perlitz, J., Pitari, G., Reddy, S., Sahu, L., Sakamoto, H., Schuster, G., Schwarz, J. P., Seland, Ø., Stier, P., Takegawa, N., Takemura, T., Textor, C., van Aardenne, J. A., and Zhao, Y.: Evaluation of black carbon estimations in global aerosol models, *Atmos. Chem. Phys.*, 9, 9001–9026, <https://doi.org/10.5194/acp-9-9001-2009>, 2009.
- Kokkola, H., Korhonen, H., Lehtinen, K. E. J., Makkonen, R., Asmi, A., Järvenoja, S., Anttila, T., Partanen, A.-I., Kulmala, M., Järvinen, H., Laaksonen, A., and Kerminen, V.-M.: SALSA – a Sectional Aerosol module for Large Scale Applications, *Atmos. Chem. Phys.*, 8, 2469–2483, <https://doi.org/10.5194/acp-8-2469-2008>, 2008.
- Kokkola, H., Kühn, T., Laakso, A., Bergman, T., Lehtinen, K. E. J., Mielonen, T., Arola, A., Stadtler, S., Korhonen, H., Ferrachat, S., Lohmann, U., Neubauer, D., Tegen, I., Siegenthaler-Le Drian, C., Schultz, M. G., Bey, I., Stier, P., Daskalakis, N., Heald, C. L., and Romakkaniemi, S.: SALSA2.0: The sectional aerosol module of the aerosol–chemistry–climate model ECHAM6.3.0-HAM2.3-MOZ1.0, *Geosci. Model Dev.*, 11, 3833–3863, <https://doi.org/10.5194/gmd-11-3833-2018>, 2018.
- Kuang, C., McMurry, P. A., M., and Eisele, F.: Dependence of nucleation rates on sulfuric acid vapor concentration in diverse atmospheric locations, *J. Geophys. Res.-Atmos.*, 113, D10209, <https://doi.org/10.1029/2007JD009253>, 2008.
- Kulmala, M., Asmi, A., Lappalainen, H. K., Baltensperger, U., Brenguier, J.-L., Facchini, M. C., Hansson, H.-C., Hov, Ø., O'Dowd, C. D., Pöschl, U., Wiedensohler, A., Boers, R., Boucher, O., de Leeuw, G., Denier van der Gon, H. A. C., Feichter, J., Krejci, R., Laj, P., Lihavainen, H., Lohmann, U., Mc-

- Figgans, G., Mentel, T., Pilinis, C., Riipinen, I., Schulz, M., Stohl, A., Swietlicki, E., Vignati, E., Alves, C., Amann, M., Ammann, M., Arabas, S., Artaxo, P., Baars, H., Beddows, D. C. S., Bergström, R., Beukes, J. P., Bilde, M., Burkhardt, J. F., Canonaco, F., Clegg, S. L., Coe, H., Crumeyrolle, S., D'Anna, B., De Cesari, S., Gilardoni, S., Fischer, M., Fjaeraa, A. M., Fouquet, C., George, C., Gomes, L., Halloran, P., Hamburger, T., Harrison, R. M., Herrmann, H., Hoffmann, T., Hoose, C., Hu, M., Hyvärinen, A., Hörrak, U., Iinuma, Y., Iversen, T., Josipovic, M., Kanakidou, M., Kiendler-Scharr, A., Kirkevåg, A., Kiss, G., Klimont, Z., Kolmonen, P., Komppula, M., Kristjánsson, J.-E., Laakso, L., Laaksonen, A., Labonnote, L., Lanz, V. A., Lehtinen, K. E. J., Rizzo, L. V., Makkonen, R., Manninen, H. E., McMeeking, G., Merikanto, J., Minikin, A., Mirme, S., Morgan, W. T., Nemitz, E., O'Donnell, D., Panwar, T. S., Pawlowska, H., Petzold, A., Pienaar, J. J., Pio, C., Plass-Duelmer, C., Prévôt, A. S. H., Pryor, S., Reddington, C. L., Roberts, G., Rosenfeld, D., Schwarz, J., Selander, Ø., Sellegri, K., Shen, X. J., Shiraishi, M., Siebert, H., Sierau, B., Simpson, D., Sun, J. Y., Topping, D., Tunved, P., Vaattovaara, P., Vakkari, V., Veefkind, J. P., Visschedijk, A., Vuollekoski, H., Vuolo, R., Wehner, B., Wildt, J., Woodward, S., Worsnop, D. R., van Zadelhoff, G.-J., Zardini, A. A., Zhang, K., van Zyl, P. G., Kerminen, V.-M., Carslaw, K., and Pandis, S. N.: General overview: European Integrated project on Aerosol Cloud Climate and Air Quality interactions (EUCAARI) – integrating aerosol research from nano to global scales, *Atmos. Chem. Phys.*, 11, 13061–13143, <https://doi.org/10.5194/acp-11-13061-2011>, 2011.
- Lacis, A. A. and Mishchenko, M. I.: Climate forcing, climate sensitivity, and climate response: A radiative modeling perspective on atmospheric aerosols, in: *Aerosols Forcing of Climate: Report of the Dahlem Workshop on Aerosol Forcing of Climate, 24–29 April 1994, Berlin*, edited by: Charlson, R. J. and Heintzenberg, J., John Wiley Sons, Chichester, England/New York, 1995.
- Lamarque, J.-F., Bond, T. C., Eyring, V., Granier, C., Heil, A., Klimont, Z., Lee, D., Liouesse, C., Mieville, A., Owen, B., Schultz, M. G., Shindell, D., Smith, S. J., Stehfest, E., Van Aardenne, J., Cooper, O. R., Kainuma, M., Mahowald, N., McConnell, J. R., Naik, V., Riahi, K., and van Vuuren, D. P.: Historical (1850–2000) gridded anthropogenic and biomass burning emissions of reactive gases and aerosols: methodology and application, *Atmos. Chem. Phys.*, 10, 7017–7039, <https://doi.org/10.5194/acp-10-7017-2010>, 2010.
- Lana, A., Bell, T. G., Simó, R., Vallina, S. M., Ballabriga-Poy, J., Kettle, A. J., Dachs, J., Bopp, L., Saltzman, E. S., Stefels, J., Johnson, J. E., and Liss, P. S.: An updated climatology of surface dimethylsulfide concentrations and emission fluxes in the global ocean, *Global Biogeochem. Cy.*, 25, GB1004, <https://doi.org/10.1029/2010GB003850>, 2011.
- Lin, S. and Rood, R.: Multidimensional Flux-Form Semi-Lagrangian Transport Schemes, *Mon. Weather Rev.*, 124, 2046–2070, [https://doi.org/10.1175/1520-0493\(1996\)124<2046:MFFSLT>2.0.CO;2](https://doi.org/10.1175/1520-0493(1996)124<2046:MFFSLT>2.0.CO;2), 1996.
- Lohmann, U. and Hoose, C.: Sensitivity studies of different aerosol indirect effects in mixed-phase clouds, *Atmos. Chem. Phys.*, 9, 8917–8934, <https://doi.org/10.5194/acp-9-8917-2009>, 2009.
- Lohmann, U. and Neubauer, D.: The importance of mixed-phase and ice clouds for climate sensitivity in the global aerosol–climate model ECHAM6-HAM2, *Atmos. Chem. Phys.*, 18, 8807–8828, <https://doi.org/10.5194/acp-18-8807-2018>, 2018.
- Lohmann, U. and Roeckner, E.: Design and performance of a new cloud microphysics scheme developed for the ECHAM general circulation model, *Clim. Dynam.*, 12, 557–572, <https://doi.org/10.1007/BF00207939>, 1996.
- Lohmann, U., Stier, P., Hoose, C., Ferrachat, S., Kloster, S., Roeckner, E., and Zhang, J.: Cloud microphysics and aerosol indirect effects in the global climate model ECHAM5-HAM, *Atmos. Chem. Phys.*, 7, 3425–3446, <https://doi.org/10.5194/acp-7-3425-2007>, 2007.
- Long, M. S., Keene, W. C., Kieber, D. J., Erickson, D. J., and Maring, H.: A sea-state based source function for size- and composition-resolved marine aerosol production, *Atmos. Chem. Phys.*, 11, 1203–1216, <https://doi.org/10.5194/acp-11-1203-2011>, 2011.
- Marticorena, B. and Bergametti, G.: Modeling the atmospheric dust cycle: 1. Design of a soil-derived dust emission scheme, *J. Geophys. Res.-Atmos.*, 100, 16415–16430, <https://doi.org/10.1029/95JD00690>, 1995.
- Myhre, G., Samset, B. H., Schulz, M., Balkanski, Y., Bauer, S., Berntsen, T. K., Bian, H., Bellouin, N., Chin, M., Diehl, T., Easter, R. C., Feichter, J., Ghan, S. J., Hauglustaine, D., Iversen, T., Kinne, S., Kirkevåg, A., Lamarque, J.-F., Lin, G., Liu, X., Lund, M. T., Luo, G., Ma, X., van Noije, T., Penner, J. E., Rasch, P. J., Ruiz, A., Selander, Ø., Skeie, R. B., Stier, P., Takemura, T., Tsigaridis, K., Wang, P., Wang, Z., Xu, L., Yu, H., Yu, F., Yoon, J.-H., Zhang, K., Zhang, H., and Zhou, C.: Radiative forcing of the direct aerosol effect from AeroCom Phase II simulations, *Atmos. Chem. Phys.*, 13, 1853–1877, <https://doi.org/10.5194/acp-13-1853-2013>, 2013.
- NASA: Level-1 and Atmosphere Archive and Distribution System Web Interface, available at: <https://ladsweb.modaps.eosdis.nasa.gov/search/>, last access: 15 May 2017.
- NASA: AERONET Data Download Tool, available at: https://aeronet.gsfc.nasa.gov/cgi-bin/webtool_opera_v2_new, last access: 1 March 2019.
- Neubauer, D., Lohmann, U., Hoose, C., and Frontoso, M. G.: Impact of the representation of marine stratocumulus clouds on the anthropogenic aerosol effect, *Atmos. Chem. Phys.*, 14, 11997–12022, <https://doi.org/10.5194/acp-14-11997-2014>, 2014.
- Neubauer, D., Ferrachat, S., Siegenthaler-Le Drian, C., Stier, P., Partridge, D. G., Tegen, I., Bey, I., Stanelle, T., Kokkola, H., and Lohmann, U.: The global aerosol-climate model ECHAM6.3-HAM2.3 – Part 2: Cloud evaluation, aerosol radiative forcing and climate sensitivity, *Geosci. Model Dev. Discuss.*, <https://doi.org/10.5194/gmd-2018-307>, in review, 2019.
- Nightingale, P. D., Malin, G., Law, C. S., Watson, A. J., Liss, P. S., Liddicoat, M. I., Boutin, J., and Upstill-Goddard, R. C.: In situ evaluation of air-sea gas exchange parameterizations using novel conservative and volatile tracers, *Global Biogeochem. Cy.*, 14, 373–387, <https://doi.org/10.1029/1999GB000091>, 2000.
- Nordeng, T. E.: Extended versions of the convective parametrization scheme at ECMWF and their impact on the mean and transient activity of the model in the tropics, Research Department Technical Memorandum, 206, 1–41, available at: <https://www.ecmwf.int/en/elibrary/11393-extended-versions-convective-parametrization-scheme-ecmwf-and-their-impact-mean> (last access: 1 March 2019), 1994.

- Norwegian Institute for Air Research: EMEP data, EBAS database, available at: <http://ebas.nilu.no/>, last access: 10 March 2015.
- O'Donnell, D., Tsigaridis, K., and Feichter, J.: Estimating the direct and indirect effects of secondary organic aerosols using ECHAM5-HAM, *Atmos. Chem. Phys.*, 11, 8635–8659, <https://doi.org/10.5194/acp-11-8635-2011>, 2011.
- Peters, K., Quaas, J., Stier, P., and Grassl, H.: Processes limiting the emergence of detectable aerosol indirect effects on tropical warm clouds in global aerosol-climate model and satellite data, *Tellus B*, 66, 24.54, <https://doi.org/10.3402/tellusb.v66.24054>, 2014.
- Petters, M. D. and Kreidenweis, S. M.: A single parameter representation of hygroscopic growth and cloud condensation nucleus activity, *Atmos. Chem. Phys.*, 7, 1961–1971, <https://doi.org/10.5194/acp-7-1961-2007>, 2007.
- Pincus, R. and Stevens, B.: Paths to accuracy for radiation parameterizations in atmospheric models, *J. Adv. Model. Earth Sy.*, 5, 225–233, <https://doi.org/10.1002/jame.20027>, 2013.
- Pozzoli, L., Bey, I., Rast, S., Schultz, M., Stier, P., and Feichter, J.: Trace gas and aerosol interactions in the fully coupled model of aeosol-chemistry-climate ECHAM5-HAMMOZ: 1. Model description and insights from the spring 2001 TRACE-P experiment, *J. Geophys. Res.-Atmos.*, 113, D07308, <https://doi.org/10.1029/2007JD009007>, 2008.
- Prospero, J. M., Uematsu, M., and Savoie, D. L.: Mineral aerosol transport to the Pacific Ocean, in: Chemical Oceanography, Vol. 10, edited by: Riley, J. P., New York, Academic Press, 137–218, 1989.
- Pruppacher, H. R. and Klett, J. D.: Microphysics of Clouds and Precipitation, Kluwer Academic, 954 pp., 1997.
- Rast, S., Schultz, M., Bey, I., van Noije, T., Aghedo, A., Brasseur, G., Diehl, T., Esch, M., Ganzeveld, L., Kirchner, I., Kornblueh, L., Rhodin, A., Roeckner, E., Schmidt, H., Schroeder, S., Schulzweida, U., Stier, P., Thomas, K., and Walters, S.: Evaluation of the tropospheric chemistry general circulation model ECHAM5-MOZ and its application to the analysis of the chemical composition of the troposphere with an emphasis on the late RETRO period 1990–2000, *Berichte zur Erdsystemforschung*, 114, 74 pp., <https://doi.org/10.17617/2.2058065>, 2014.
- Reick, C., Raddatz, T., Brovkin, V., and Gayler, V.: Representation of natural and anthropogenic land cover change in MPI-ESM, *J. Adv. Model. Earth Sy.*, 5, 459–482, <https://doi.org/10.1002/jame.20022>, 2013.
- Roeckner, E., Baeuml, G., Bonaventura, L., Brokopf, R., Esch, M., Giorgetta, M., Hagemann, S., Kirchner, I., Kornblueh, L., Manzini, E., Rhodin, A., Schlese, U., Schulzweida, U., and Tompkins, A.: The atmospheric general circulation model ECHAM5. Part I: Model description, Max-Planck-Inst. Tech. Report, 349, ISSN 0937 - 1060, 140 pp., 2003.
- Schepanski, K., Tegen, I., Todd, M., Heinold, B., Boenisch, G., Laurent, B., and Macke, A.: Meteorological processes forcing Saharan dust emission inferred from MSG SE-VIRI observations of subdaily dust source activation for numerical models, *J. Geophys. Res.-Atmos.*, 114, D10201, <https://doi.org/10.1029/2008JD010325>, 2009.
- Schultz, M. G., Stadtler, S., Schröder, S., Taraborrelli, D., Franco, B., Krefting, J., Henrot, A., Ferrachat, S., Lohmann, U., Neubauer, D., Siegenthaler-Le Drian, C., Wahl, S., Kokkola, H., Kühn, T., Rast, S., Schmidt, H., Stier, P., Kinnison, D., Tyndall, G. S., Orlando, J. J., and Wespes, C.: The chemistry-climate model ECHAM6.3-HAM2.3-MOZ1.0, *Geosci. Model Dev.*, 11, 1695–1723, <https://doi.org/10.5194/gmd-11-1695-2018>, 2018.
- Schutgens, N., Tsyro, S., Grispeerd, E., Goto, D., Weigum, N., Schulz, M., and Stier, P.: On the spatio-temporal representativeness of observations, *Atmos. Chem. Phys.*, 17, 9761–9780, <https://doi.org/10.5194/acp-17-9761-2017>, 2017.
- Schutgens, N. A. J. and Stier, P.: A pathway analysis of global aerosol processes, *Atmos. Chem. Phys.*, 14, 11657–11686, <https://doi.org/10.5194/acp-14-11657-2014>, 2014.
- Schutgens, N. A. J., Partridge, D. G., and Stier, P.: The importance of temporal collocation for the evaluation of aerosol models with observations, *Atmos. Chem. Phys.*, 16, 1065–1079, <https://doi.org/10.5194/acp-16-1065-2016>, 2016.
- Seifert, A. and Beheng, K. D.: A two-moment cloud microphysics parameterization for mixed-phase clouds. Part 1: Model description, *Meteorol. Atmos. Phys.*, 92, 45–66, <https://doi.org/10.1007/s00703-005-0112-4>, 2006.
- Seinfeld, J. and Pandis, S.: Atmospheric Chemistry and Physics: From Air Pollution to Climate Change, Wiley, Publisher Wiley New York, 1326 pp., 1998.
- Shi, Y., Zhang, J., Reid, J. S., Hyer, E. J., Eck, T. F., Holben, B. N., and Kahn, R. A.: A critical examination of spatial biases between MODIS and MISR aerosol products – application for potential AERONET deployment, *Atmos. Meas. Tech.*, 4, 2823–2836, <https://doi.org/10.5194/amt-4-2823-2011>, 2011.
- Sinyuk, A., Torres, O., and Dubovik, O.: Combined use of satellite and surface observations to infer the imaginary part of refractive index of Saharan dust, *Geophys. Res. Lett.*, 30, 1081, <https://doi.org/10.1029/2002GL016189>, 2003.
- Slinn, S. and Slinn, W.: Predictions for particle deposition on natural waters, *Atmos. Environ.*, 14, 1013–1016, 1980.
- Smirnov, A., Holben, B. N., Slutsker, I., Giles, D. M., McClain, C. R., Eck, T. F., Sakerin, S. M., Macke, A., Croot, P., Zibordi, G., Quinn, P. K., Sciare, J., Kinne, S., Harvey, M., Smyth, T. J., Piketh, S., Zielinski, T., Proshutinsky, A., Goes, J. I., Nelson, N. B., Larouche, P., Radionov, V. F., Goloub, P., Krishna Moorthy, K., Matarrese, R., Robertson, E. J., and Jourdin, F.: Maritime Aerosol Network as a component of Aerosol Robotic Network, *J. Geophys. Res.-Atmos.*, 114, D06204, <https://doi.org/10.1029/2008JD011257>, 2009.
- Sofiev, M., Soares, J., Prank, M., deLeeuw, G., and Kukkonen, J.: A regional to global model of emission and transport of sea salt particles in the atmosphere, *J. Geophys. Res.-Atmos.*, 116, D21302, <https://doi.org/10.1029/2010JD014713>, 2011.
- Stanelle, T., Bey, I., Raddatz, T., Reick, C., and Tegen, I.: Anthropogenically induced changes in twentieth century mineral dust burden and the associated impact on radiative forcing, *J. Geophys. Res.-Atmos.*, 119, 13526–13546, <https://doi.org/10.1002/2014JD022062>, 2014.
- Stevens, B., Giorgetta, M., Esch, M., Mauritsen, T., Crueger, T., Rast, S., Salzmann, M., Schmidt, H., Bader, J., Block, K., Brokopf, R., Fast, I., Kinne, S., Kornblueh, L., Lohmann, U., Pincus, R., Reichler, T., and Roeckner, E.: Atmospheric component of the MPI-M Earth System Model: ECHAM6, *J. Adv. Model. Earth Sy.*, 5, 146–172, <https://doi.org/10.1002/jame.20015>, 2013.
- Stier, P., Feichter, J., Kinne, S., Kloster, S., Vignati, E., Wilson, J., Ganzeveld, L., Tegen, I., Werner, M., Balkanski, Y., Schulz, M., Boucher, O., Minikin, A., and Petzold, A.: The aerosol-climate

- model ECHAM5-HAM, *Atmos. Chem. Phys.*, 5, 1125–1156, <https://doi.org/10.5194/acp-5-1125-2005>, 2005.
- Stier, P., Seinfeld, J. H., Kinne, S., and Boucher, O.: Aerosol absorption and radiative forcing, *Atmos. Chem. Phys.*, 7, 5237–5261, <https://doi.org/10.5194/acp-7-5237-2007>, 2007.
- Stier, P., Schutgens, N. A. J., Bellouin, N., Bian, H., Boucher, O., Chin, M., Ghan, S., Huneeus, N., Kinne, S., Lin, G., Ma, X., Myhre, G., Penner, J. E., Randles, C. A., Samset, B., Schulz, M., Takemura, T., Yu, F., Yu, H., and Zhou, C.: Host model uncertainties in aerosol radiative forcing estimates: results from the AeroCom Prescribed intercomparison study, *Atmos. Chem. Phys.*, 13, 3245–3270, <https://doi.org/10.5194/acp-13-3245-2013>, 2013.
- Sundqvist, H., Berge, E., and Kristjansson, J.: Condensation and Cloud Parameterization Studies with a Mesoscale Numerical Weather Prediction Model, *Mon. Weather Rev.*, 117, 1641–1657, [https://doi.org/10.1175/1520-0493\(1989\)117<1641:CACPSW>2.0.CO;2](https://doi.org/10.1175/1520-0493(1989)117<1641:CACPSW>2.0.CO;2), 1989.
- Taylor, K. E., Williamson, D., and Zwiers, F.: AMIP II Sea Surface Temperature and Sea Ice Concentration Boundary Conditions, vol. 60, PCMDI Report No. 60, 20 pp., 2000.
- Tegen, I., Harrison, S. P., Kohfeld, K. E., Prentice, I. C., Coe, M., and Heimann, M.: Impact of vegetation and preferential source areas on global dust aerosol: Results from a model study, *J. Geophys. Res.-Atmos.*, 107, AAC 14–1–AAC 14–27, <https://doi.org/10.1029/2001JD000963>, 2002.
- Textor, C., Schulz, M., Guibert, S., Kinne, S., Balkanski, Y., Bauer, S., Berntsen, T., Berglen, T., Boucher, O., Chin, M., Dentener, F., Diehl, T., Easter, R., Feichter, H., Fillmore, D., Ghan, S., Ginoux, P., Gong, S., Grini, A., Hendricks, J., Horowitz, L., Huang, P., Isaksen, I., Iversen, I., Kloster, S., Koch, D., Kirkevåg, A., Kristjansson, J. E., Krol, M., Lauer, A., Lamarque, J. F., Liu, X., Montanaro, V., Myhre, G., Penner, J., Pitari, G., Reddy, S., Seland, Ø., Stier, P., Takemura, T., and Tie, X.: Analysis and quantification of the diversities of aerosol life cycles within AeroCom, *Atmos. Chem. Phys.*, 6, 1777–1813, <https://doi.org/10.5194/acp-6-1777-2006>, 2006.
- Textor, C., Schulz, M., Guibert, S., Kinne, S., Balkanski, Y., Bauer, S., Berntsen, T., Berglen, T., Boucher, O., Chin, M., Dentener, F., Diehl, T., Feichter, J., Fillmore, D., Ginoux, P., Gong, S., Grini, A., Hendricks, J., Horowitz, L., Huang, P., Isaksen, I. S. A., Iversen, T., Kloster, S., Koch, D., Kirkevåg, A., Kristjansson, J. E., Krol, M., Lauer, A., Lamarque, J. F., Liu, X., Montanaro, V., Myhre, G., Penner, J. E., Pitari, G., Reddy, M. S., Seland, Ø., Stier, P., Takemura, T., and Tie, X.: The effect of harmonized emissions on aerosol properties in global models – an AeroCom experiment, *Atmos. Chem. Phys.*, 7, 4489–4501, <https://doi.org/10.5194/acp-7-4489-2007>, 2007.
- Tiedtke, M.: A Comprehensive Mass Flux Scheme for Cumulus Parameterization in Large-Scale Models, *Mon. Weather Rev.*, 117, 1779–1800, [https://doi.org/10.1175/1520-0493\(1989\)117<1779:ACMFSF>2.0.CO;2](https://doi.org/10.1175/1520-0493(1989)117<1779:ACMFSF>2.0.CO;2), 1989.
- Val Martin, M., Logan, J. A., Kahn, R. A., Leung, F.-Y., Nelson, D. L., and Diner, D. J.: Smoke injection heights from fires in North America: analysis of 5 years of satellite observations, *Atmos. Chem. Phys.*, 10, 1491–1510, <https://doi.org/10.5194/acp-10-1491-2010>, 2010.
- van Vuuren, D. P., Edmonds, J., Kainuma, M., Riahi, K., Thomson, A., Hibbard, K., Hurtt, G. C., Kram, T., Krey, V., Lamarque, J.-F., Masui, T., Meinshausen, M., Nakicenovic, N., Smith, S. J., and Rose, S. K.: The representative concentration pathways: an overview, *Climatic Change*, 109, 5–31, <https://doi.org/10.1007/s10584-011-0148-z>, 2011.
- Veira, A., Kloster, S., Schutgens, N. A. J., and Kaiser, J. W.: Fire emission heights in the climate system – Part 2: Impact on transport, black carbon concentrations and radiation, *Atmos. Chem. Phys.*, 15, 7173–7193, <https://doi.org/10.5194/acp-15-7173-2015>, 2015.
- Vignati, E., Wilson, J., and Stier, P.: M7: An efficient size resolved aerosol microphysics module for large scale aerosol transport, *J. Geophys. Res.-Atmos.*, 109, D22202, <https://doi.org/10.1029/2003JD004485>, 2004.
- Watson-Parris, D., Schutgens, N., Winker, D., Burton, S. P., Ferrell, R. A., and Stier, P.: On the limits of CALIOP for constraining modelled free-tropospheric aerosol, *Geophys. Res. Lett.*, 45, 9260–9266, <https://doi.org/10.1029/2018gl078195>, 2018.
- Zhang, J. and Reid, J. S.: MODIS aerosol product analysis for data assimilation: Assessment of over-ocean level 2 aerosol optical thickness retrievals, *J. Geophys. Res.-Atmos.*, 111, D22207, <https://doi.org/10.1029/2005JD006898>, 2006.
- Zhang, K., O'Donnell, D., Kazil, J., Stier, P., Kinne, S., Lohmann, U., Ferrachat, S., Croft, B., Quaas, J., Wan, H., Rast, S., and Feichter, J.: The global aerosol-climate model ECHAM-HAM, version 2: sensitivity to improvements in process representations, *Atmos. Chem. Phys.*, 12, 8911–8949, <https://doi.org/10.5194/acp-12-8911-2012>, 2012.